

Review

Linking Powder Properties, Printing Parameters, Post-Processing Methods, and Fatigue Properties in Additive Manufacturing of AlSi10Mg

Ritam Pal  and Amrita Basak * 

Department of Mechanical Engineering, Pennsylvania State University, University Park, PA 16802, USA

* Correspondence: aub1526@psu.edu

Abstract: Additive manufacturing (AM) of metals can be broadly accomplished via two defined technologies: powder bed fusion and directed energy deposition. During AM fabrication, the melted feedstock material experiences fast thermal cycling due to the layer-by-layer deposition process resulting in microstructures and properties that are drastically different from the traditionally manufactured parts. For AM to become a viable process for fabricating critical components made of high-performance structural alloys, such as AlSi10Mg, a comprehensive understanding is required toward developing the process-structure-property relationships prevalent in AM. AlSi10Mg, with its good castability, strength, hardness, and dynamic properties, is typically used to fabricate structural components that are required to withstand high loads. This alloy has been consolidated predominantly by the laser powder bed fusion (L-PBF) method and several critical mechanical properties, such as fatigue, have been reported to date. This article, first, summarizes the as-deposited and heat-treated microstructures of AlSi10Mg specimens fabricated by L-PBF. Then, the article discusses the linkages among the feedstock properties, printing parameters, specimen geometry, post-processing techniques, and fatigue properties. This discussion is followed by a section on the fatigue life prediction of AlSi10Mg specimens using computational modeling. Finally, the article identifies critical research gaps and pinpoints future research opportunities.

Keywords: additive manufacturing; laser powder bed fusion; AlSi10Mg; fatigue properties; process-structure-fatigue property linkages



Citation: Pal, R.; Basak, A. Linking Powder Properties, Printing Parameters, Post-Processing Methods, and Fatigue Properties in Additive Manufacturing of AlSi10Mg. *Alloys* **2022**, *1*, 149–179. <https://doi.org/10.3390/alloys1020010>

Academic Editor: Sangbong Yi

Received: 13 April 2022

Accepted: 29 June 2022

Published: 28 July 2022

Publisher's Note: MDPI stays neutral with regard to jurisdictional claims in published maps and institutional affiliations.



Copyright: © 2022 by the authors. Licensee MDPI, Basel, Switzerland. This article is an open access article distributed under the terms and conditions of the Creative Commons Attribution (CC BY) license (<https://creativecommons.org/licenses/by/4.0/>).

1. Introduction

AlSi10Mg is a hardenable aluminum-based alloy that possesses appreciable hardness and dynamic toughness [1,2]. This alloy is extensively used in fabricating structural parts, such as brackets, brake caliper, and heat sinks [2]. The alloy's high thermal conductivity and resistance to corrosion make it suitable for aerospace and automotive applications [3]. AlSi10Mg can retain its high strength while undergoing dynamic loads [3]. Typically, AlSi10Mg components are fabricated using casting. However, with the advent of additive manufacturing (AM), AlSi10Mg components are increasingly being manufactured via AM as well. AM offers significant advantages over casting because of its ability to fabricate complex multi-functional parts with reduced material waste [4]. AM components also require less thermal post-processing than cast components [2]. Due to its structural applications, it is imperative to obtain certifiable mechanical properties of AlSi10Mg irrespective of whether it is consolidated via casting or AM.

Based on the classification put forth by the American Society for Testing and Materials (ASTM), metal AM has four main subcategories, namely, powder bed fusion (PBF), directed energy deposition (DED), binder jetting (BJ), and sheet lamination [5]. Among all these subcategories, DED and PBF are the most proven and feasible methods for metals [6]. In DED, the energy source and the material feeding nozzles are focused at the deposition site [7]. The feeding nozzles provide the material in the form of wire or powder, and the

energy source melts the material on the surface of the deposit site creating a small melt pool. In PBF, a coating roller spreads out the powder on the building platform [8]. An energy source selectively melts the top few layers of the powder. Once the upper layers are fused and solidified, the build platform is lowered for the next coating of powder. In PBF, two different energy sources can be implemented, such as, a laser or an electron beam. The laser-based powder bed fusion (L-PBF) is a popular PBF process that has shown remarkable capabilities in processing AlSi10Mg. In L-PBF, a thin layer of powder is selectively melted and consolidated by using a high-energy laser beam, as shown in Figure 1. Printing parameters, such as the scan pattern [9], laser power [10], scanning speed [11], hatch spacing [12], layer thickness [10], build orientation [13,14], and build plate temperature [15] are typically varied to produce parts with the desired characteristics, such as surface quality [9,10], porosity [16,17], dimensional accuracy [18,19], microstructures (e.g., columnar vs. equiaxed grain) [20–22], and properties (e.g., mechanical [23–25], hardness [26–28], corrosion [11,29], and oxidation [13,30,31]).

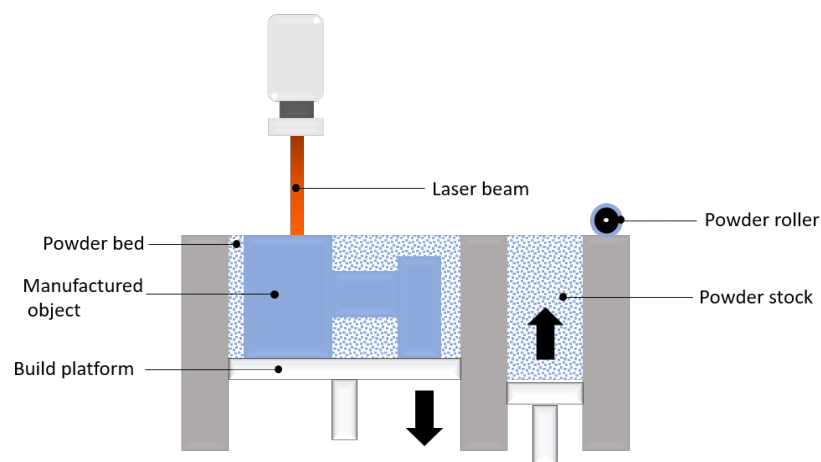


Figure 1. Schematic of an L-PBF process.

Among different alloys that have been successfully processed using L-PBF, a significant volume of work exists with AlSi10Mg [15,32,33]. In AM, the feedstock (e.g., virgin vs. recycled, etc.) and the printing parameters (e.g., high vs. low cooling rates, etc.) dictate the as-built deposit properties (e.g., pores, microstructures, anisotropy, etc.). These properties affect the heat treatment response and the mechanical properties (e.g., tensile, fatigue, etc.) of the final part (Figure 2). To advance the fundamental linkages among all these critical steps (Figure 2), this article aims to present an overview of how fatigue properties of the L-PBF-fabricated AlSi10Mg specimens are affected by the feedstock properties, printing parameters, specimen geometries, and post-processing treatments. Both ex-situ and in-situ experimental approaches are discussed in details. Thereafter, the article summarizes the state-of-the-art computational modeling results that are crucial in developing predictive capability.

The paper is divided into seven sections, including the present one. Section 2 surveys the properties of the feedstock material. Section 3 discusses the deposit characteristics of the AlSi10Mg parts fabricated via L-PBF. Specifically, the focus is on understanding the impact of powder properties, printing parameters, solidification microstructure, and post-processing on the deposit quality. Section 4 reveals the impact of porosities, printing parameters, post-processing, and loading conditions on the fatigue properties of AlSi10Mg specimens. For the sake of clarity and consistency, in this article, the defects imply *cracks* whereas the porosities imply *gas pores* including *surface and subsurface pores* and *lack of fusion pores*. Section 5 summarizes the state-of-the-art research involving in-situ fatigue testing that can shed critical insights on how fatigue damages initiate and propagate. Section 6 articulates the computational modeling-based methods that can predict the fatigue life of

AlSi10Mg specimens fabricated via L-PBF. Section 7 provides a summary of the existing work and identifies future research opportunities.

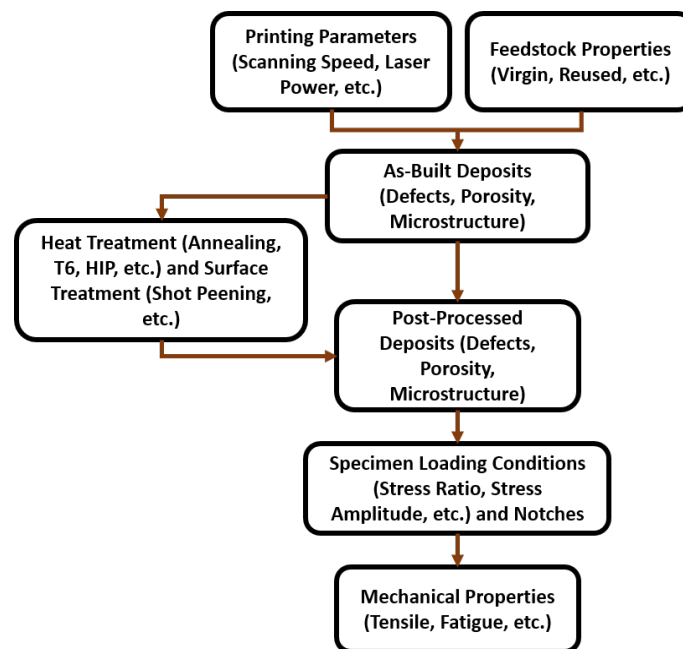


Figure 2. Overview of the process–structure–post-process–property relationships in L-PBF of AlSi10Mg.

2. Feedstock Properties

General Overview: The existing literature uses AlSi10Mg powders produced by several different powder manufacturers, such as EOS GmbH [34], ECKA granules [35], SLM solutions group Ag [33], and LPW technology [32]. The properties of these powders are summarized in Table 1. AlSi10Mg primarily consists of Aluminum (Al). The amounts of Silicon (Si) and Magnesium (Mg) vary in the alloy (Table 2). Other elements, such as Iron (Fe), Nitrogen (N), Oxygen (O), Titanium (Ti), Zinc (Zn), Manganese (Mn), Nickel (Ni), Copper (Cu), Lead (Pb), and Tin (Sn) are also present, but they contribute to less than 1 wt. % of the composition. AlSi10Mg powders are primarily produced by gas atomization involving argon or nitrogen [36]. In L-PBF, the powder morphology is also critical as it dictates the flowability [37,38]. The morphology and the particle size distribution are typically characterized by optical microscopy (OM), scanning electron microscopy (SEM), and X-ray diffraction (XRD) [39]. The Electron Dispersive X-ray Spectroscopy (EDS) method is utilized to determine the elemental distribution in the powder particles [39].

Existing works have attempted to optimize the atomization process to obtain the desired powder properties [39,40]. The length of the metal delivery tube and the gas flow rate and gas pressure are found to impact the powder properties. Increasing the gas flow rate or gas pressure decreases the average particle size and the range of the particle size distribution [41]. The length of the metal delivery tube, on the contrary, has little effect on the particle size [42]. A decrease in the tube diameter leads to the formation of smaller particles [39].

Li et al. [43] investigated the impact of the inner diameter of the melt nozzles on the particle size distribution during gas atomization. With a decrease in the diameter, the upper limit of the particle size distribution was reduced to less than 40 μm . However, a reduction in the diameter increased the flow resistance and the viscous pressure drop within the metal delivery tube. To overcome the flow resistance and the viscous pressure drop, an external driving force was required to achieve the desired metal flow. Hence, an over-pressure unit along with a nozzle heating unit was employed. The new system produced finer particles like the conventional gas atomization process, however, with a smaller diameter nozzle and, therefore, increased the yield.

Table 1. Properties of AlSi10Mg powders obtained from different manufacturers.

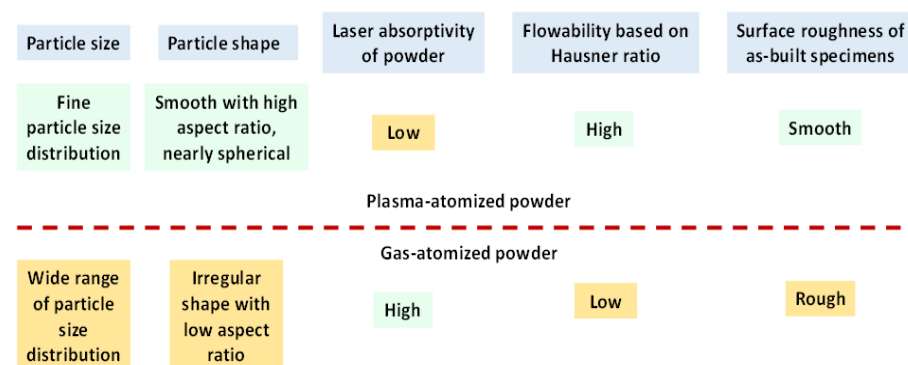
Manufacturer	Particle Size (μm)	Mass Density (g/cm^3)	Thermal Conductivity ($\text{W}/(\text{m}\cdot\text{K})$)
SLM solutions group Ag [44]	20–63	2.67	130–150
EOS GmbH [3]	25–70	2.67	100–110

Table 2. Chemical composition of the AlSi10Mg powders (in wt. %).

Al	Si	Mg	Fe	N	O	Ti	Zn	Mn	Ni	Cu	Pb	Sn
Balance	9–11	0.25–0.45	<0.25	<0.2	<0.2	<0.15	<0.1	<0.1	<0.05	<0.05	<0.02	<0.02

Gas-Atomized vs. Plasma-Atomized Powder: Riener et al. studied the impact of powder particle size and morphology on the powder properties, such as the flowability and the laser power absorption [45]. This study compared several batches of gas-atomized and plasma-atomized AlSi10Mg virgin powders. The authors used SEM to characterize the particle shape and morphology, followed by the dynamic image analysis method to obtain the particle size distribution. The flowability was determined by a granular material density analyzer which reported the Hausner ratio. A Hausner ratio of 1–1.1 indicates an excellent flowability followed by a good flowability range of 1.12–1.18 and a fair flowability range of 1.19–1.25 [46]. The laser power absorption was determined via ultraviolet-visible spectroscopy.

The plasma-atomized powders were found to be more spherical compared to the gas-atomized powders. The gas-atomized powders had oxide inclusions and satellite attachments on their surfaces, whereas the plasma-atomized powders were smooth and did not have any oxide inclusions or satellites. Particles below 10 μm diameter were found in the plasma-atomized powders, however, the gas-atomized powder had a particle size distribution range of 10 μm to 100 μm . Dynamic image analysis revealed that the plasma-atomized powder had a higher aspect ratio approaching an ideal spherical shape, unlike the gas-atomized powder. The plasma-atomized powder also possessed a lower Hausner ratio indicating improved flowability. The presence of spherical particles increased the packing density. Hence, both bulk and tap density of the powder increased. The laser power absorption was found to improve due to the presence of fine particles in the plasma-atomized powder. The particle shape also affected the laser power absorption. Non-spherical particles showed a higher laser power absorption coefficient indicating that the gas-atomized powder with a fine particle size distribution and irregular shapes would result in high laser power absorption. An overview of the properties of the plasma-atomized and gas-atomized powders is presented in Figure 3.

**Figure 3.** Overview of powder properties obtained by gas and plasma atomization.

Impact of the Gas Atomization Parameters: Chu et al. compared two batches of the gas-atomized powders produced under different temperature and pressure environment [47].

Batch 1 was produced under a melt superheat of 180 °C and a gas pressure of 1.8×10^6 Pa while Batch 2 was produced under a melt superheat of 110 °C and a gas pressure of 3.5×10^6 Pa. SEM micrographs showed Batch 1 particles to be more spherical than Batch 2 as depicted in Figure 4a,b. Hence, Batch 1 had higher flowability and packing density, and reduced cohesion than Batch 2. Batch 2 particles showed agglomeration and satellites, as shown in Figure 4c,d. The presence of the satellite particles increased the equivalent diameter and reduced the sphericity. Hence, Batch 2 had a wider particle size distribution than Batch 1 as illustrated in Figure 4e. Seven distinct rheological properties [37,48,49] were measured and compared:

1. Basic Flow Energy (BFE): The required flow resistance energy during the anticlockwise rotation of the bulldozing blade down through the powder bed.
2. Specific Energy (SE): The blade energy required to move upward through the powder bed.
3. Aeration Energy (AE): The blade rotation resistance energy required to move through the aerated powder bed base.
4. Consolidation Flow Energy (CFE): The energy needed to overcome the resistance of blade rotation in the powder consolidated by controlled tapping.
5. Conditioned Bulk Density (CBD): The bulk density of powders in natural state.
6. Compressibility Index (CI): The ratio of the compressed powder density to the conditioned bulk density.
7. Cohesion Stress (CS): The shear stress that initiates powder flow.

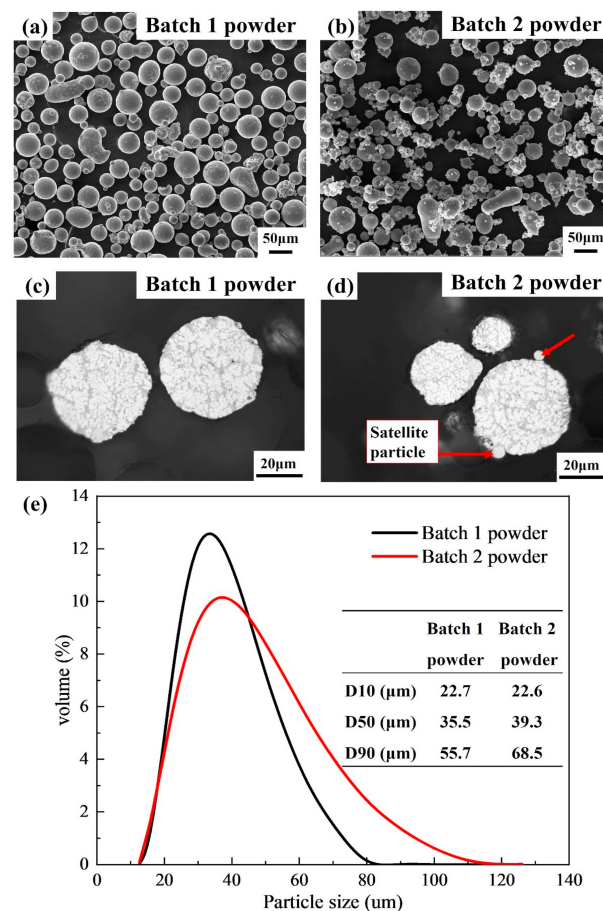


Figure 4. SEM images of (a) Batch 1 powder and (b) Batch 2 powder. Polished cross-sections showing (c) spherical particles in Batch 1 powder and (d) satellite particles in Batch 2 powder. (e) The particle size distribution of Batch 1 and Batch 2 powders. Reprinted with permission from Ref. [47]. Copyright 2021 Elsevier.

An FT4 rheometer was used in measuring the rheological properties of the powders [48,50]. The results showed that BFE, AE, CI, and CE were much lower for Batch 1 compared to Batch 2. It was mainly because of the presence of non-spherical particles in Batch 2. Batch 1 had a lower CS and a higher CBD, resulting in a more uniform and dense powder layer during L-PBF. In summary, the powder batch atomized at 180 °C and 1.8×10^6 Pa pressure was found to be ideal for L-PBF processing.

Impact of Powder Reuse: Powders are often recycled in L-PBF to reduce the cost of manufacturing. With an increase in the number of reuse cycle, the oxygen content in the powder increases. The shape of the recycled powder particles shows deformation during L-PBF as they start to agglomerate. The recycled powder also shows satellites. Moreover, there is a loss of fine particles with an increase in the number of reuse cycles because the powder particles are sintered during the L-PBF process [51]. Representative SEM images of the virgin and recycled powders are shown in Figure 5. Tradowsky et al. reported that the pore area increased with the number of reuse cycle. The virgin powder had 0.26% pore area, whereas the reused powder showed 2% pore area [52].

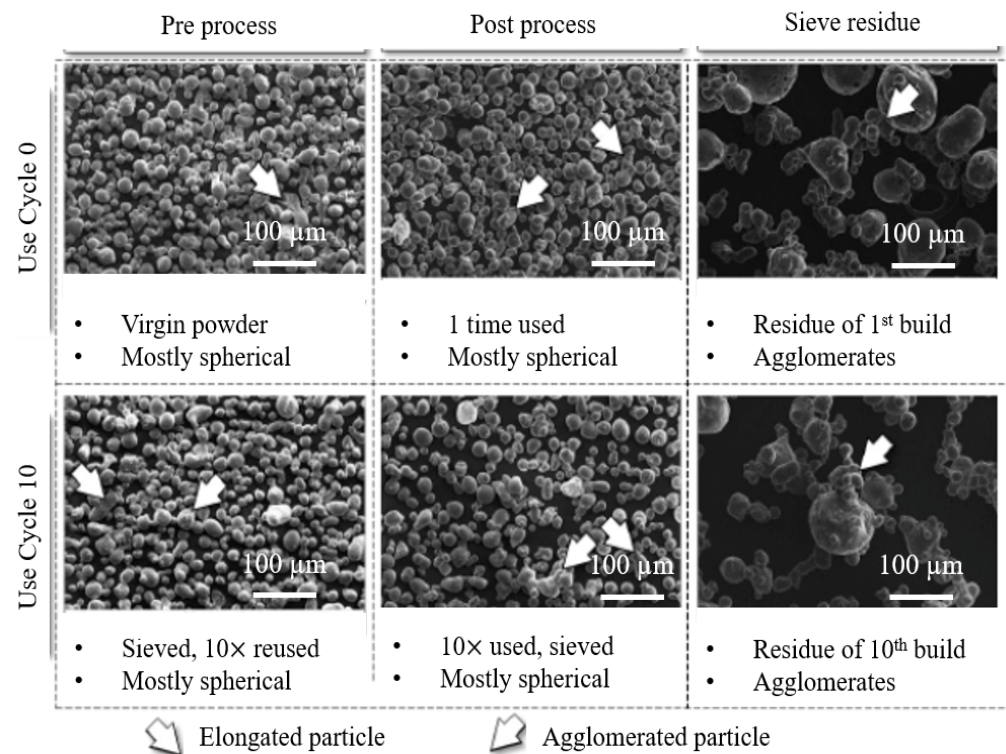


Figure 5. Representative SEM images of the AlSi10Mg powders: pre-process (**left**), post-process and sieved (**middle**), and sieved residue (**right**) for the virgin powder (**upper**) and 10th use cycle (**lower**). Reprinted with permission from Ref. [51]. Copyright 2021 Laboratory for Freeform Fabrication and University of Texas at Austin.

3. Deposit Characteristics

Impact of Powder Properties: The particle morphology and the particle size distribution were found to affect the surface roughness of L-PBF specimens. The plasma-atomized powder contained spherical particles that reduced the surface roughness. Hence, AlSi10Mg specimens fabricated using plasma-atomized powder showed low surface roughness [45]. On the other hand, a particle size distribution having finer particles created a rough surface because the finer particles were found to adhere to the melt pool boundary. However, no differences were observed in the part densities of the specimens built using different powders. The reused gas-atomized powder showed high oxygen content on the particle surfaces. Additionally, the AlSi10Mg powders were found to pick up oxygen once exposed to the atmosphere. When these powders were reused, the oxygen content of the specimens

increased. Such a rise in oxygen content was confirmed by the SEM/EDX analysis of specimens built using reused AlSi10Mg powder, as shown in Figure 6.

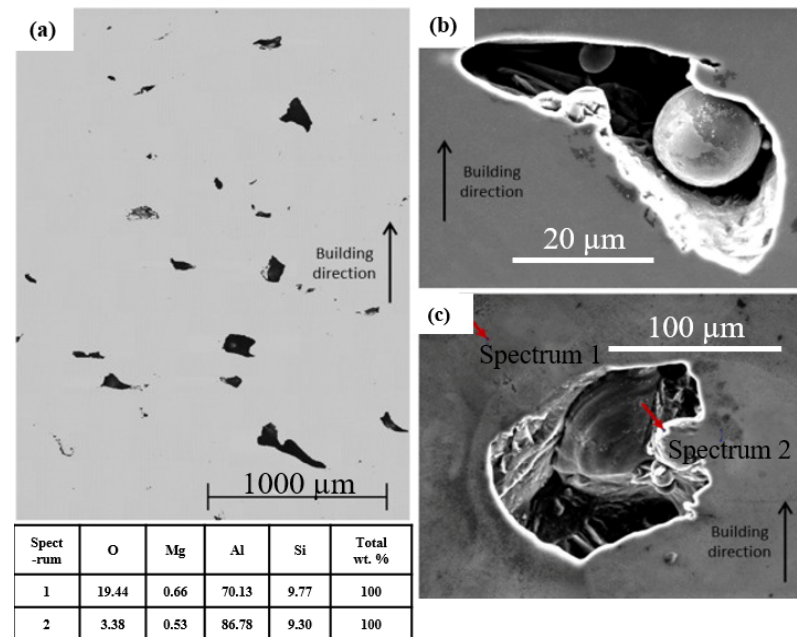


Figure 6. Pores in the as-built specimens: (a) OM image of the pore distribution and orientation, (b) SEM image of a representative pore with entrapped powder particles, and (c) SEM/EDX analysis of a wavy pore surface (Spectrum 1) compared with the matrix (Spectrum 2). Reprinted with permission from Ref. [52]. Copyright 2016 Elsevier.

Impact of Printing Parameters: In L-PBF, the temperature gradient across the melt pool gives rise to the surface tension gradient resulting in the Marangoni convection. A lower scanning speed allows for more interaction between the laser source and the material. Hence, the peak surface temperature and the temperature gradient increase. An increase in the temperature gradient may initiate turbulence making the solid–liquid interface unstable. The L-PBF-processed AlSi10Mg specimens typically show a semi-circular melt pool, however, the shape may vary with printing parameters. Wei et al. studied the impact of laser power and scanning speed on the stability of the scan tracks [53]. Low scanning speeds exposed the material to such a high temperature that some elements were lost due to evaporation [54]. The porosity of the specimens was found to be a function of the surface stability of the scan track [55]. Additionally, the scanning speed and laser power were also observed to affect the formation of pores. Representative OM images of AlSi10Mg specimens fabricated using different laser powers and scanning speeds: are shown in Figure 7. It is evident that certain combinations of the printing parameters decrease the formation of pores (Figure 7a,d,e). Hence, an optimization of the printing parameters is essential to avoid a large number of pores in the printed parts. For example, the lack of fusion porosity may arise from the insufficient overlap between melt pools. The as-built specimens typically reveal re-melting of four layers in some areas. A contrast in the melt pool boundary (Figure 7) implies the presence of microstructural inhomogeneities due to high thermal gradients.

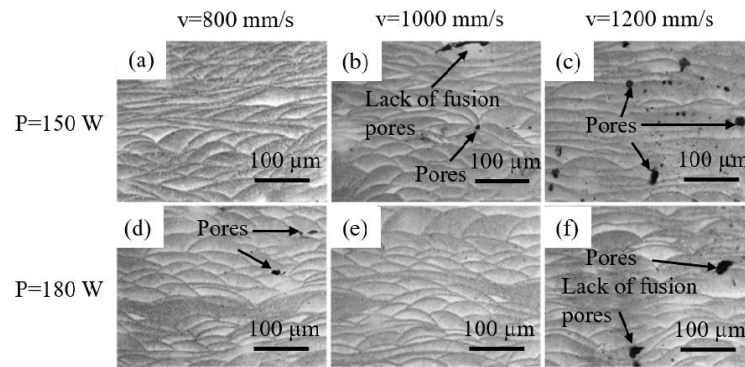


Figure 7. OM images showing the melt pool morphology of AlSi10Mg specimens processed at different laser power and scanning speeds. Here, 'P' represents the laser power and 'v' represents the scanning speed. Reprinted/adapted with permission from Ref. [53]. Copyright 2017 Elsevier.

Solidification Microstructure: It is critical to understand the solidification process in L-PBF to decipher the microstructure evolution. For AlSi10Mg, the solidification process starts with Si. Si then enters into the liquid phase at the solid–liquid interface. Due to the rapid cooling rates prevalent in L-PBF, the solubility of Si in Al increases which further decreases the Si content in the liquid phase. Hence, after solidification, a supersaturated Al-rich microstructure typically forms with the residual Si at the boundaries [56,57]. SEM and EDX images are found to confirm these solidification paths as shown in Figure 8a [53]. Figure 8b shows the Al-rich microstructure. The presence of Si at the boundaries is shown in Figure 8c. Mg reacts with Si to form Mg_2Si phase at the cellular boundaries that can be observed in Figure 8d. SEM images also indicate that a eutectic cellular network is present in L-PBF AlSi10Mg specimens [58]. These eutectic ribbons are found to be Si-rich.

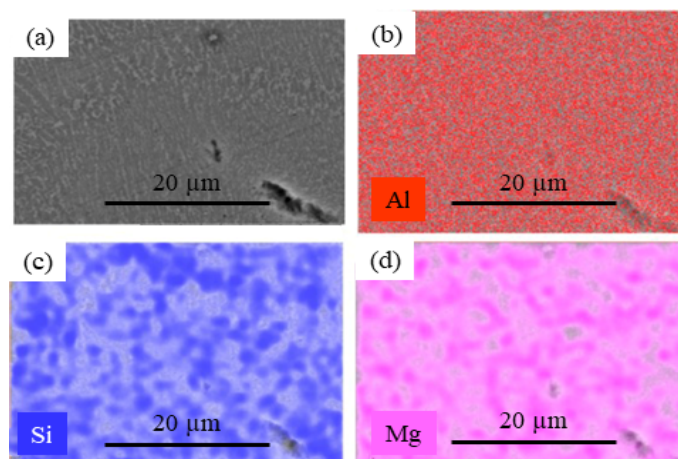


Figure 8. (a) SEM image of a representative AlSi10Mg specimen with EDX maps of (b) Al, (c) Si, and (d) Mg. Reprinted with permission from Ref. [53]. Copyright 2017 Elsevier.

Impact of Post-Processing: Fite et al. investigated the impact of solution treatment on the microstructure of AlSi10Mg specimens [59]. The solution heat treatment at 530 °C was found to disband the eutectic ribbons and facilitate the formation of microscale Si precipitates. Takata et al. compared the as-built, annealed, and solution heat-treated microstructures of AlSi10Mg specimens [60]. The as-built specimens showed a characteristic half-cylindrical melt pool shape like other works [61–63]. The specimens also showed columnar Al grains in the melt pool. Annealing at 300 °C for 2 h made the Si particles coarser in some parts. Fine Si particles were found to be within the columnar Al grains implying that the Si phase precipitated within the Al matrix during annealing. However, after the solution treatment at 530 °C for 6 h, the melt pool boundaries were not visible

via an optical microscope. The Si particles also became significantly coarser. The solution treatment caused the formation of Fe intermetallic phases with a rod-shaped morphology. The coarsening of Si particles was also observed in the AlSi10Mg specimens subjected to hot isostatic pressing (HIP) [64]. A relatively longer holding time at 530 °C allowed more diffusion of the Si particles making them less abundant.

4. Fatigue Properties

4.1. Effect of Powder Reuse

The cost of the virgin AlSi10Mg powder can range from USD 80 to USD 120 per kilogram [65]. Reusing powders can reduce the manufacturing cost by thousands of dollars [66]. To investigate the impact of powder recycling, Del Re et al. conducted a study to understand the mechanical properties of AlSi10Mg specimens manufactured using virgin and reused powders [67]. The excess powder from the build chamber was collected by a conveyor module, and sieved using a 60 µm mesh. The powder was then re-loaded into the printer to build new parts. The weight percentages of the major elements were significantly affected. With an increase in the number of reuse cycles, the ultimate tensile strength decreased by 3%, while the high-cycle fatigue strength decreased by 12%. It was concluded that the powder could be reused a number of times without affecting the fatigue properties appreciably. However, this conclusion is hypothesized to be material- and machine-dependent.

4.2. Effect of Porosity

Fatigue life is severely compromised due to the presence of porosity [68–70]. Ferro et al. studied the effect of porosities on the fatigue properties of L-PBF AlSi10Mg specimens [71]. Fatigue tests were carried out on a multiaxial test machine having a maximum load of 50 kN. Post-testing, the specimens were analyzed to characterize porosities (Figure 9). The results showed that fatigue cracks initiated from the surface pores of the specimens. Fractography analysis revealed the lack-of-fusion porosities to be the critical ones. Large and irregular lack of fusion porosities posed more threat to fatigue life than the well-distributed regular-shaped porosities. Laursen et al. established a correlation between the ductility and porosity of AlSi10Mg specimens [72]. The results showed that the ductility decreased linearly with an increase in the surface porosity (Figure 10). At higher porosities, there was hardly any necking in the specimen, implying that the specimen showed brittle fracture. Apart from correlation-based models, other methods, such as the 'Index of Defect Susceptibility' model [73] and the 'Critical Local Strain' model [74] were also employed to determine the correlation between ductility and porosity. Figure 11 shows the impact of fracture surface porosity on the ductility of as-built AlSi10Mg specimens.

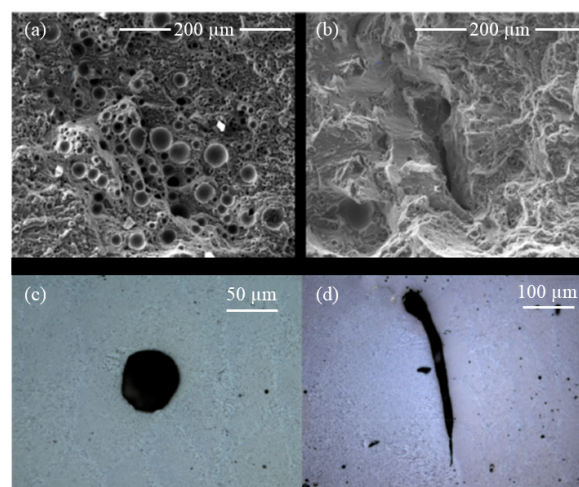


Figure 9. (a,c) Representative gas porosities. (b,d) Lack of fusion porosities. Reprinted with permission from Ref. [71]. Copyright 2020 Elsevier.

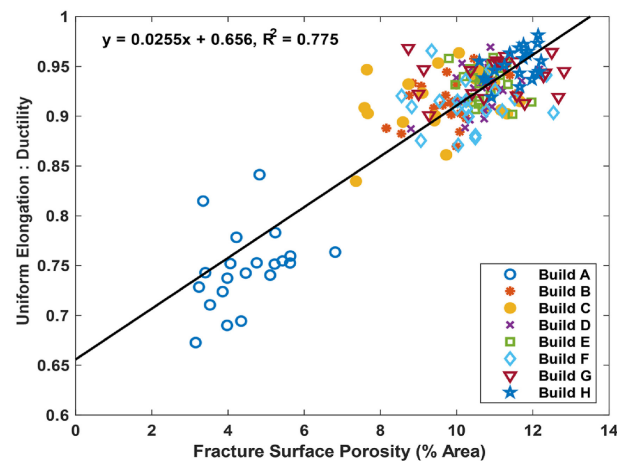


Figure 10. Ratio of uniform elongation to ductility as a function of fracture surface porosity. Build A was produced with fresh powders. Builds B through E were produced with recycled powders where the number of reuse cycle was varied from 1 to 4, respectively. In Build F, the machine was filled with new powder that had been stored for several weeks in an argon environment. Builds G and H were produced with recycled powder where the number of reuse cycle was varied from 1 to 2 starting from F. Reprinted with permission from Ref. [72]. Copyright 2020 Elsevier.

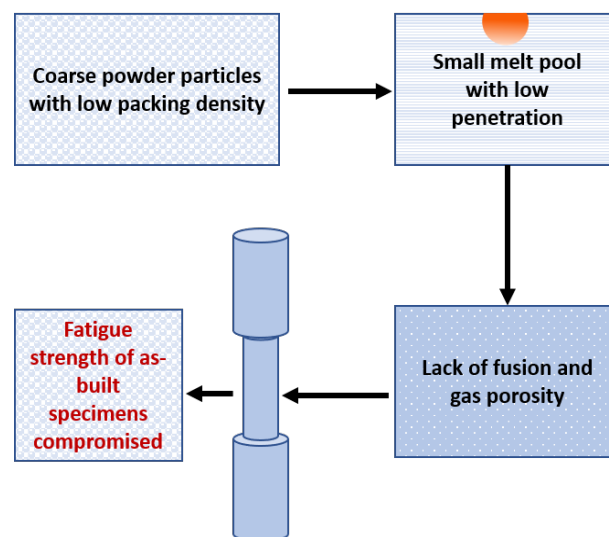


Figure 11. Schematic depicting the impact of porosity on fatigue strength.

4.3. Effect of Printing Parameters and Build Direction

The L-PBF process involves more than 150 printing parameters that can be calibrated to optimize the part properties [75]. The energy density parameter that combines the laser power, scanning speed, layer thickness, and hatch spacing is a well-known measure [76]. In some machines, the hatch distance is always fixed. Hence, this parameter was not varied in several studies [77]. Olakanmi et al. investigated the impact of printing parameters on the porosities [78]. The scanning speed was varied between 20 to 250 mm/s and the laser power was altered between 20 to 240 W with a constant hatching distance of 0.1 mm. The combinations of the printing parameters resulted in four types of deposit characteristics: (i) at a very low energy density, no bonding between the powder particles was observed; (ii) at a low energy density, small, open, and deep porosities were present; (iii) at an optimized energy density, the deposit was dense; and (iv) at a very high energy density, melt track balling and instability were prominent.

Brandao et al. correlated the fatigue properties of AlSi10Mg specimens with the layer thickness and build orientation [79]. Horizontal and vertical build orientations were

selected, and for each orientation, specimens were built with two different layer thicknesses, e.g., 30 μm and 90 μm . The specimens built with 30 μm layer thickness consisted of a smaller number of pores compared with the specimens built with 90 μm layer thickness. A larger layer thickness implies a lower energy density which causes lack-of-fusion porosities. These pores within the layers act as imperfections giving rise to stress concentrations, which reduce the fatigue strength of the specimens. Hence, the specimens built with 30 μm layer thickness showed a higher fatigue strength than the specimens built with 90 μm layer thickness [79].

Tang et al. fabricated AlSi10Mg specimens with varying hatch spacing and build directions [80]. Three different hatch spacings were considered: 0.16 mm, 0.19 mm, and 0.22 mm. The build directions were horizontal and vertical. The fatigue resistance of specimens with a larger hatch spacing was lower than those with a smaller hatch spacing. A larger hatch spacing induced more lack-of-fusion pores that acted as the stress concentration factors from which the fatigue cracks initiated. Large pores were present in the specimens built with a larger hatch spacing. However, a significant number of small pores were present in the specimens built with a smaller hatch spacing due to a higher number of melting cycles. The remelting process did not eliminate the pores but reduced their sizes. The specimens built along the horizontal direction showed slightly more fatigue resistance than those built along the vertical direction. This was due to the pores being parallel to the stress direction for the horizontally-built specimens. For the vertically-built specimens, the pores were perpendicular to the stress direction. The surface roughness of the specimens was found to depend on the build direction [81]. The specimen surface perpendicular to the build direction showed crater-like structures. Beevers et al. fabricated AlSi10Mg specimens with and without contours [82]. The fatigue strength of the specimens without contour was significantly more than those with contour because the surface roughness of the specimens without contour was found to be lower. Moreover, the specimens without contour showed a higher compressive residual stress which enhanced the fatigue strength. A summary of the fatigue testing results performed by Beevers et al. is shown in Figure 12 [82].

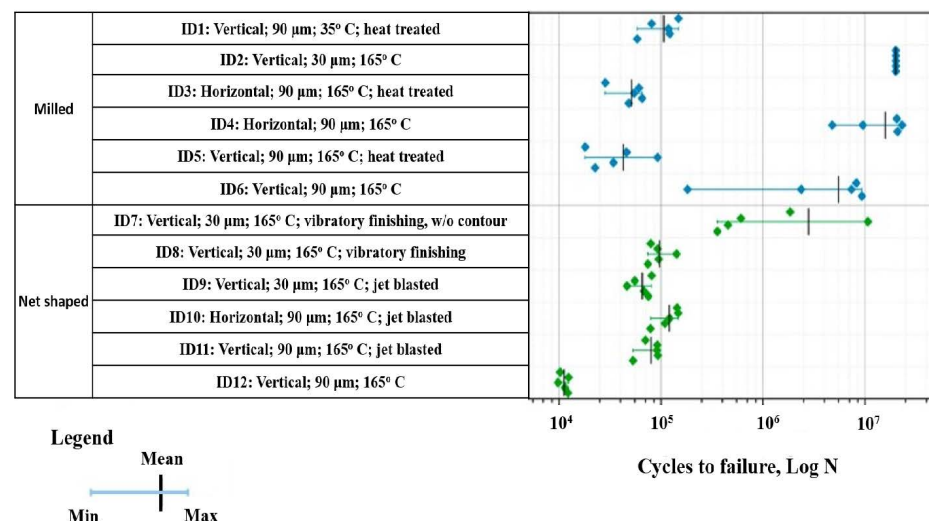


Figure 12. Impact of contour and build direction on the fatigue resistance of AlSi10Mg. Fatigue testing was conducted at a stress amplitude of 120 MPa and with a stress ratio of -1 . Reprinted/adapted with permission from Ref. [82]. Copyright 2018 Elsevier.

Brandl et al. investigated the fatigue properties of several AlSi10Mg specimens having build directions of 0° , 45° , and 90° , as shown in Figure 13. Two different build platform temperatures, i.e., 30 $^\circ\text{C}$ and 300 $^\circ\text{C}$, were used in conjunction with a peak-hardening procedure for a handful of specimens once they were built [15]. The results showed that the peak-hardening process increased the fatigue resistance of the specimens built along the 0° direction compared to the other two build directions for the build platform

temperature of 30 °C (Figure 14). However, when the build platform was at 300 °C, the peak hardening process significantly increased the fatigue resistance of specimens built along the 45°, and 90° directions. The specimens without peak hardening showed the lowest fatigue strength. The pores in the specimens built along the 45° and 90° directions were not parallel to the stress direction. These pores, therefore, gave rise to stress concentrations.



Figure 13. Static-tensile specimens built in different directions: (a) 0°, (b) 45°, and (c) 90°. Reprinted with permission from Ref. [15]. Copyright 2012 Elsevier.

From statistical analysis, it was concluded that the build direction had the least impact on the fatigue properties. The highest impact was caused by the peak hardening procedure. The hardening process eliminated the microstructural inhomogeneities present in the heat-affected zones and caused the interdendritic eutectic Si particles to become spheroidal. These spheroidal particles obstructed crack initiation. Hence, they were aptly termed as ‘crack arresters’ [83]. A higher build platform temperature reduced the cooling rates and residual stresses. Thus, fewer defects were present, leading to higher fatigue strengths. The fatigue strength was significantly higher for the T6 specimens built along the 45° and 90° directions for the build platform temperature of 300 °C compared to that of 30 °C build platform temperature as summarized in Table 3. With an increase in the build platform temperature, the pores inside the specimens disappeared, enhancing the fatigue resistance. It is evident from the results that the pores induce breakthrough fatigue cracks and there are articles that support the presence of anisotropy of specimens depending on the building direction [84–86]. Thus, one way to improve the fatigue resistance of AlSi10Mg specimens would be by reducing or eliminating pores.

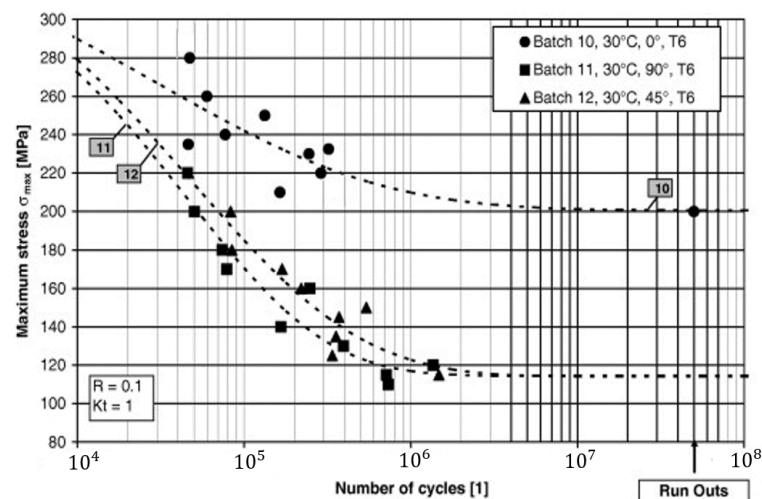


Figure 14. Fatigue resistance and Weibull distribution (50% probability of failure) of specimens built at 30 °C platform temperature. Reprinted with permission from Ref. [15]. Copyright 2012 Elsevier.

4.4. Effect of Heat Treatment and Surface Treatment

Aboulkhair et al. evaluated four types of AlSi10Mg specimens: as-built, as-built + machined, heat-treated, and heat-treated + machined [32,87]. The heat treatment process was carried out following a conventional T6 procedure: solution heat treatment for 1 h at 520 °C followed by water quenching to the room temperature and, then, artificial aging

for 6 h at 160 °C [88]. The conventional T6 procedure enhanced the tensile strength and hardness of AlSi10Mg specimens according to many literature [89]. The microstructures of the as-built and heat-treated specimens are compared in Figure 15. The heat-treated specimens showed an appreciable increase in the fatigue strength compared to the as-built specimens. The as-built specimens reached a nominal cycle limit of 3×10^7 under a maximum stress of 63 MPa, whereas the heat-treated specimens reached a nominal cycle limit at maximum stress of 157 MPa.

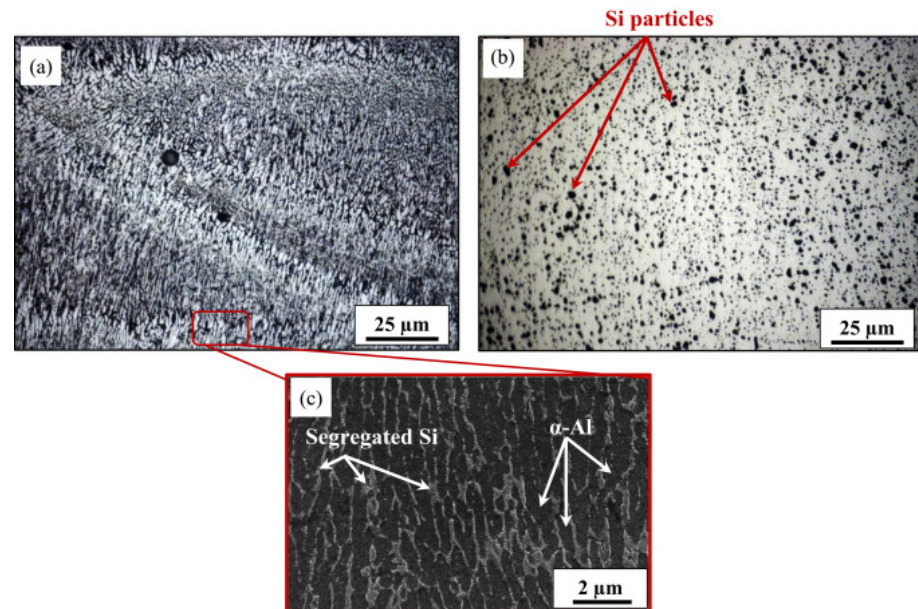


Figure 15. Representative optical images of AlSi10Mg in the (a) as-built and (b) heat-treated conditions. (c) High-magnification SEM image of the as-built microstructure revealing Si segregation on the boundaries of α -Al. Reprinted with permission from Ref. [32]. Copyright 2016 Elsevier.

The heat-treated + machined specimens did not show any significant change to the stress–number of cycle (S-N) curve when compared with the heat-treated specimens. Fractography analysis revealed microstructure coarsening after heat treatment making the material more ductile and, therefore, increasing the fatigue strength (Figure 16). The results also revealed that the machining process exposed the sub-surface porosities. Since the fatigue cracks were found to originate and propagate from those porosities, overall, the effect of machining was negligible. The study concluded that a well-designed heat treatment procedure could significantly improve the fatigue strength without requiring any machining. This conclusion is particularly useful for complex geometries that are difficult to machine.

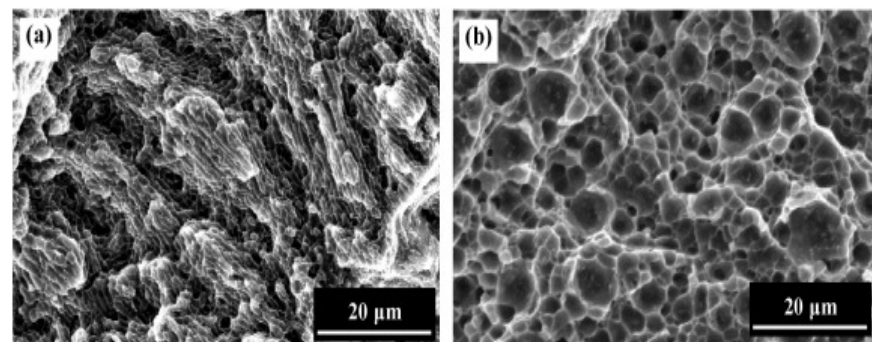


Figure 16. High magnification SEM images of the fractured surfaces of the (a) as-built and (b) heat-treated specimens. Reprinted with permission from Ref. [32]. Copyright 2016 Elsevier.

Several studies reported the efficacy of combining heat treatment processes with other post-treatment methods to improve the fatigue strength. Bagherifard et al. employed kinetic surface treatments, such as sandblasting and shot peening (SP), along with the T6 heat treatment process on L-PBF AlSi10Mg specimens [33]. Prior to heat treatment, the as-built specimens showed a significant amount of surface roughness and non-homogeneous microstructure arising from the scan tracks. The heat treatment process improved the microstructure by making it homogeneous and eliminating the heat-affected zones. The fatigue strength of the heat-treated specimens improved by 50% compared to the as-built specimens. Overall, the kinetic surface treatments resulted in smoother surfaces by partially closing the surface pores. When these surface treatments were applied to the as-built specimens, the fatigue strength was enhanced by a whopping 270%. However, on applying these surface treatments to the heat-treated specimens, the kinetic energy caused multiple pores on the surfaces leading to a degradation of the fatigue strength. Mild shot peening (SP) is, therefore, hypothesized to be more appropriate for heat-treated specimens, however, the parameters need to be optimized.

Tocci et al. reported a novel high-pressure heat treatment procedure of AlSi10Mg specimens [64]. Four different types of heat treatments, such as annealing, conventional T6 heat treatment, hot isostatic pressing followed by the T6 treatment (HIP + T6), and high-pressure T6 treatment (HP + T6), were performed. HIP, carried out at 500 °C in the Argon atmosphere at a pressure of 75–150 MPa, improved the ductility and toughness of the specimens but decreased the hardness, strength, and fatigue resistance [90]. A complete T6 treatment was required after HIP to obtain the necessary mechanical properties [52,91]. During the heat treatment procedure, occasionally, pores were found to open, and oxide particles were observed to form [92,93]. Thus, the study explored the possibility of implementing a single-step high-pressure heat treatment procedure that would take place in the HIP vessel. This novel HP + T6 treatment process was carried out by performing the HIP process, followed by quenching using a cooling gas inside the HIP vessel. Thereafter, the specimens were reheated to an aging temperature of 165 °C for 4 h while maintaining the pressure at 150 MPa.

SEM analysis of the AlSi10Mg specimens revealed that annealing did not cause any significant changes to the as-built microstructures of the specimens, but the other heat treatment procedures caused the Si particles to become coarser and spherical. The coarsening occurs due to the diffusion of Si atoms at high temperatures. The diffusion phenomena in AlSi10Mg was found to be a function of the duration, temperature, and pressure of the post-treatment processes [32,94]. SEM images further showed that annealing destroyed the network of interconnected Si particles, which was present in the as-built specimens. Digital image analysis depicted that large Si particles were present in the HIP + T6 specimens, however, they were less abundant. The coarsening behavior of the Si particles was found to be similar for both the HP + T6 and T6 specimens. In conclusion, the high-pressure process did not affect the coarsening of Si particles. It was observed that the part density was the highest for the HP + T6 specimens, followed by the HIP + T6 specimens. The annealed and T6 specimens possessed the lowest part density. The ultimate tensile strength decreased for all heat-treated specimens, but the yield strength increased for all except annealing. The yield strength was maximum for the HIP + T6 specimens, followed by the T6, HP + T6, and as-built specimens. Fractography analysis showed that pores were sparse in the HIP specimens, but they were abundant in the as-built, annealed, and T6 specimens. Representative fractured surfaces of all specimens are presented in Figure 17. In conclusion, HP + T6 and HIP + T6 were found to achieve similar mechanical properties. However, HP + T6 is advantageous over HIP + T6 because it takes less time. Hence, HP + T6 is a good alternative to ensure high part density and improved mechanical properties.

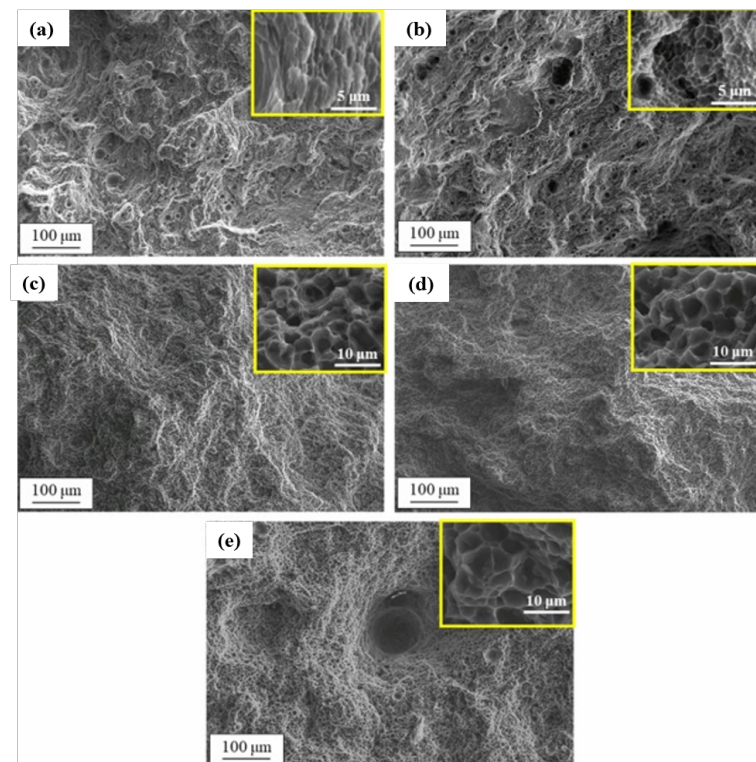


Figure 17. Fracture surfaces of specimens built in the horizontal direction: (a) as-built, (b) annealed, and after (c) HP + T6, (d) HIP + T6, and (e) T6 treatment. The magnified images are provided in the yellow boxes located at the top right corner. Reprinted with permission from Ref. [64]. Copyright 2020 Springer Nature.

Uzan et al. evaluated the fatigue strength of as-built, stress-relieved, and stress-relieved + HIP AlSi10Mg specimens [95]. HIP, conducted at 500 °C, decreased the ultimate tensile strength and fatigue strength of the material but increased its ductility. After HIP, depressions or dimples appeared on the specimen surfaces increasing the surface roughness. The fatigue strength was the lowest for the stress-relieved + HIP specimens. Fractography analysis depicted that the fatigue crack surface was planar. No microtears were observed in the as-built specimens. However, the microtears became more prominent in the stress-relieved specimens where the tearing plane was perpendicular to the direction of crack propagation. The stress-relieved + HIP specimens showed fatigue cracks similar to the ductile fracture with dimples created on the fracture surfaces. Schneller et al. emphasized the effects of HIP on the fatigue strength of AlSi10Mg specimens [96]. HIP treatment above the solubility temperature with a low-temperature annealing was found to enhance the fatigue strength of the specimens by 64%. The treatment resulted in Si agglomeration, which resisted crack growth by interfering with the crack front, thus, improving the fatigue strength. HIP also altered the failure mechanisms. In the as-built specimens, pores were responsible for failure, but in the HIP specimens, the inter-metallic in-homogeneity was responsible for failure. A summary of the results is tabulated in Table 3.

Table 3. A summary of literature on printing parameter variation and post-processing treatments.

Literature	Heat Treatment	Printing Parameters					Fatigue Strength at 10 ⁶ Cycles	
		Type	Spot Size	Power	Scan Speed	Layer Thickness	Build Direction	
Brandl et al. [15]	No	Nd:YAG laser, Trumpf TrumaForm LF130 powder-bed	0.2 mm	250 W	500 mm/s	50 µm	0° (Platform temp. 300 °C)	100–120 MPa
							45° (Platform temp. 300 °C)	100 MPa
	90° (Platform temp. 300 °C)						100 MPa	
	Yes						0° (Platform temp. 30 °C)	210 MPa
							45° (Platform temp. 30 °C)	120 MPa
	90° (Platform temp. 30 °C)						120 MPa	
	0° (Platform temp. 300 °C)						160 MPa	
	45° (Platform temp. 300 °C)						160 MPa	
	90° (Platform temp. 300 °C)						160 MPa	
	Maskery et al. [97]						No	Renishaw AM250 machine
Yes		134 MPa						
Aboulkhair et al. [32]	No	Renishaw AM250 machine	68 µm	200 W	571 mm/s	25 µm	90°	65 MPa
	Yes							130 MPa
Bagherifard et al. [33]	No	Renishaw AM250 machine	78 µm	350 W	1150 mm/s	78 µm	90°	50 MPa
	Yes							75 MPa
Re et al. [67]	Yes	EOSINT M280 system	100 µm	400 W	-	-	0°	188 MPa
							45°	177 MPa
							90°	177 MPa
							0° (3 times reused powder)	172 MPa
							0° (8 times reused powder)	188 MPa

The impact of SP on fatigue has been investigated by several researchers. The types of shots used in SP can impact the mechanical properties of the specimens [98,99]. Two different types of materials were reported to be used for SP: Gp165 glass beads (high-intensity SP) and Gp50 glass beads (low-intensity SP). Although SP using Gp165 led to the formation of microcracks, Gp50 resulted in a better surface finish, and it eliminated the microcracks present on the machined surfaces. High compressive residual stresses were found on the shot-peened surfaces. An in-depth analysis showed that the maximum compressive stress was of order 170 ± 7 MPa at a depth of 90 μm . SP was also found to impact the melt pool characteristics. The melt pool was observed to have a significant deformation after SP. Maamoun et al. investigated the influence of the SP intensity variation on the microstructure of the AlSi10Mg specimens [99]. High-intensity SP of the machined surfaces impacted the melt pool at large depths. It also created circular stress waves, which originated from the shot contact position and continued to a depth of 10 μm . The stress wave patterns were not present in the specimens subjected to low-intensity SP. The application of high-pressure waves during SP caused microstructure refinement by disintegrating the fibrous Si network and forming nanoscale Si precipitates. Hence, SP was advantageous in enhancing the fatigue performance of L-PBF AlSi10Mg specimens [33,95,100].

AlSi10Mg specimens fabricated via L-PBF typically exhibit excellent static strengths. Unfortunately, their performance under dynamic loading is lackluster because of the limited ductility and, the presence of tensile residual stress, porosity, and poor surface morphology. Mechanical and/or electrochemical surface polishing methods can be used to address some of these challenges. However, these processes can occasionally lead to inconsistent results. Additionally, they involve extra costs. Polishing specimen surfaces using both mechanical and electrochemical methods led to significant improvements in the fatigue resistance [101]. The corrosion tests showed that the fatigue life of unpolished specimens was lower compared to the polished specimens [101]. Laser shock peening is another way of improving the fatigue strength of specimens [102]. Figure 18 summarizes the impact of several critical parameters on the fatigue strength of L-PBF AlSi10Mg.

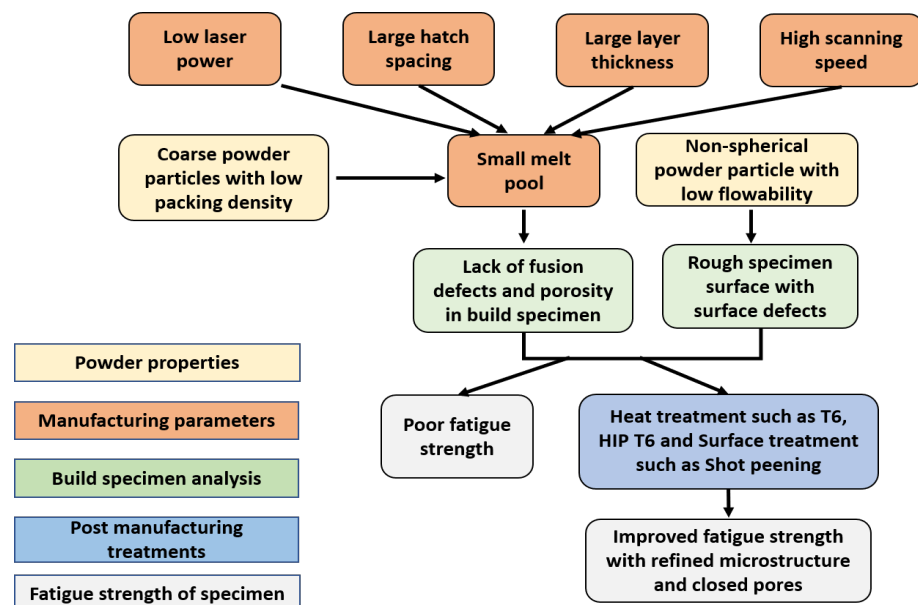


Figure 18. A schematic illustrating the impact of powder properties and printing parameters on the fatigue properties.

4.5. Impact of Loading Conditions

Awd et al. performed fatigue tests of AlSi10Mg specimens at two different load cycle frequencies: 20 Hz and 20 kHz [103]. At 20 Hz, stress-controlled tests were performed for different stress amplitudes. The second set of tests was conducted at 20 kHz using a

ultrasonic fatigue testing equipment. The main objective of this very high-frequency test was to evaluate the fatigue properties of the specimens under high-cycle and very high-cycle fatigue loading conditions. When ultrasonic vibration was applied, the temperature of the specimens increased rapidly, requiring high-pressure dry air to cool the specimens. At a stress amplitude of 140 MPa, the testing frequency did not have any impact on the number of cycles to failure. However, when the stress amplitude was decreased below 120 MPa, the testing frequency started to impact the fatigue life of the specimens. The influence of microstructure was more dominant in the low-cycle fatigue regime, while in the high-cycle fatigue regime, the pores had more impact. It was revealed that the microstructures could recommence the crack propagation during high cycle fatigue loading. Awd et al. also investigated the impact of build platform temperature. The first set of specimens was manufactured without heating the build platform, while the second set of specimens was fabricated with a build platform temperature of 200 °C. The specimens built on a heated platform had a higher fatigue life than those built on a non-heated platform.

Romano et al. focused on the low-cycle fatigue behavior of AlSi10Mg specimens [104]. Fatigue tests were performed at a frequency of 0.5 Hz and a stress ratio -1 . The defect size, in the range of 0.1 mm to 0.3 mm, was found to be critical in both high- and low-cycle fatigue regimes [105]. Multiple crack initiation sites were found on the specimen surfaces. A significant amount of strain localization was observed around the cracks as well. This strain localization was found to evolve with time. The crack nucleation time was found to be longer compared to the crack propagation time in the low-cycle fatigue regime [106,107]. Zhang et al. evaluated the performance of AlSi10Mg specimens under high-cycle and very high-cycle fatigue loading conditions [108]. The stress ratio played an important role in the high-cycle and the very high-cycle fatigue regimes. An increase in the stress ratio resulted in a decrease in fatigue strength. The presence of pores reduced the fatigue strength drastically by an order of 2. Qian et al. studied the effect of mean stress during high-cycle and very high-cycle fatigue testing of AlSi10Mg specimens [109]. The specimens were manufactured with the optimized printing parameters, but stochastic internal pores were present. These pores acted as the crack initiation sites in the very high-cycle fatigue regime. The effect of build direction and mean stress on the fatigue strength is summarized in Figure 19.

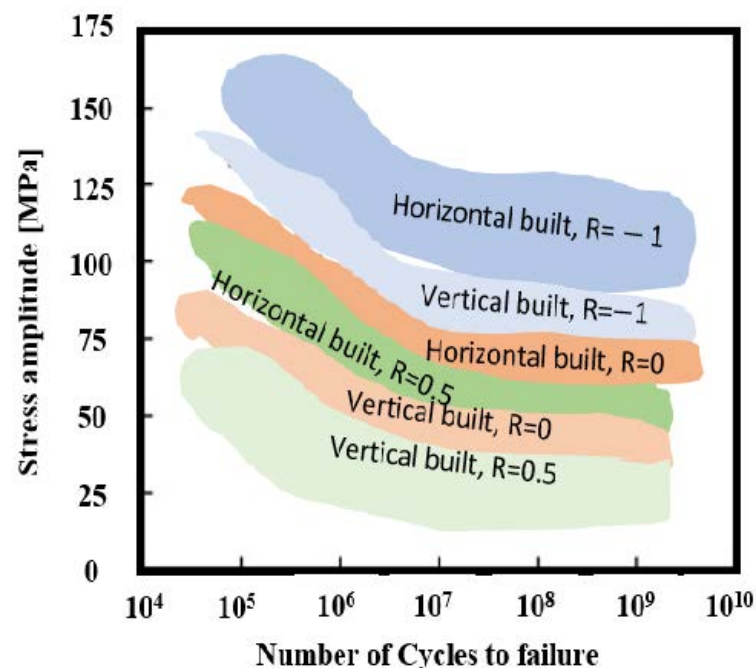


Figure 19. A plot of stress amplitude vs. number of cycles to failure for AlSi10Mg specimens fabricated with different orientations and tested under different stress ratios [109].

Tridello et al. investigated the fatigue failure characteristics of AlSi10Mg specimens under very high-cycle fatigue loading conditions [110]. The authors reported that fatigue failure might occur at lower stress amplitudes due to the presence of large pores similar to high-cycle fatigue conditions. A cluster of pores was found to be the major contributor to fatigue failure of the specimens. The pores present in the region closer to the specimen surface proved to be very critical in dictating the fatigue failure in the very high-cycle fatigue regime. The work pointed out that 2D metallographic inspection might be misleading in predicting the fatigue life of specimens as an accurate 3D size distribution of pores is required.

4.6. Impact of Notch

The presence of a notch can drastically affect the fatigue properties of AlSi10Mg specimens. To compare the fatigue strengths of un-notched and notched specimens, a notch sensitivity factor is typically defined [100]. A notch sensitivity factor (q) of 0 implies that the specimen is not influenced by the notch. For $q = 1$, it indicates that the fatigue strength is dependent on the notch. The notch sensitivity factor is obtained from the fatigue notch factor and the stress concentration factor. The fatigue notch factor is the ratio of the fatigue limits of un-notched specimen to a notched specimen. Fatigue strength is influenced by the plastic strain accumulation around the notch. Nicoletto et al. attempted to quantify the effects of a notch on the fatigue strength of AlSi10Mg specimens manufactured by the L-PBF process [111]. Miniature specimens were used to evaluate the fatigue properties. The results showed that the notched specimens were very sensitive to the direction of the applied stresses with respect to their build orientation. The performance of the worst and best directions differed by 100%. On the contrary, for un-notched specimens, the difference was 60%. The horizontally-built specimens showed a notch sensitivity factor of 0 indicating that the fatigue strengths of un-notched and notched specimens built in that direction were similar.

Maleki et al. compared the fatigue strengths of notched and un-notched AlSi10Mg specimens processed with different heat treatments and surface treatments [100]. Images of representative sub-surface porosities are shown in Figure 20. The surface treatment involved two different materials, e.g., steel and ceramic. For the as-built specimens, q was found to be greater than 1 due to the presence of surface porosity around the primary notch. These porosities acted like secondary notches. SP treatments appreciably reduced the surface porosity, thus, decreasing q . The heat treatment process contributed to the homogenization of the microstructure. The combination of heat treatment and SP with steel particles drastically reduced the q value to 0.05, implying that a notched specimen would have a similar fatigue limit as an un-notched specimen. Fractography analysis revealed that the crack initiation sites for the as-built specimens were the surface porosities around the notch. Heat and SP treatment processes shifted the crack initiation zone closer to the notch root. A compilation of the fatigue strengths for different types of specimens is summarized in Table 4.

Table 4. Fatigue strengths corresponding to 3×10^6 cycles for different specimens. Reprinted with permission from Ref. [100]. Copyright 2022 Elsevier.

Specimen Type	Fatigue Strength (MPa)
Notched As-Built	6
Notched Heat-Treated	45
Notched As-Built + SP with steel	92
Notched As-Built + SP with ceramic	100
Notched Heat-Treated + SP with steel	95
Notched Heat-Treated + SP with ceramic	110
Smooth As-Built	50
Smooth Heat-Treated	75
Smooth As-Built+SP with steel	185
Smooth Heat-Treated + SP with steel	102

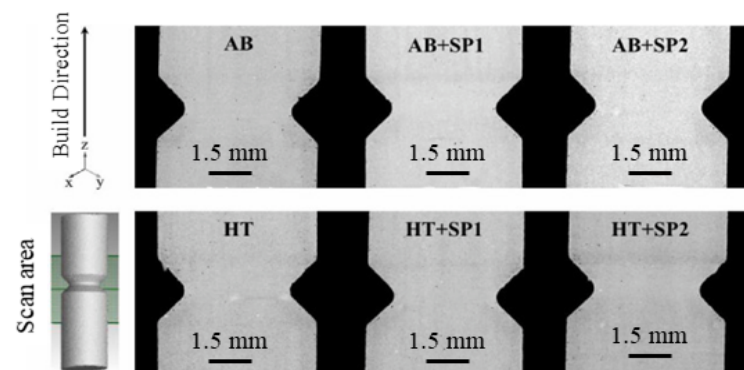


Figure 20. CT images of the sub-surface porosities around the notches. Reprinted with permission from Ref. [100]. Copyright 2022 Elsevier.

5. In-Situ Fatigue Testing

An ability to visualize pores and how they evolve during fatigue testing can play a critical role in understanding the failure characteristics of AlSi10Mg specimens. Much of the existing work has focused on analyzing the specimens before and after fatigue testing. Before fatigue testing, the specimens can be inspected using computed tomography (CT) to evaluate the distribution of pores inside the specimens. After fatigue testing, fractography analysis can be conducted to investigate the fracture surfaces to understand how a specimen may have failed. However, a thorough knowledge of the failure mechanisms can only be obtained by capturing the time-lapse images of the pore evolution during fatigue testing. Qian et al. performed fatigue testing inside CT machine using a custom-designed equipment [112]. From the 3D CT scan images, the fatigue crack propagation process was quantified. An elliptical crack front with a relatively flat crack propagation path was observed. The fatigue crack was detected after 300,000 cycles, and the crack resulted in fracture after an additional 34,587 loading cycles. When two off-plane cracks were growing simultaneously, the bridging ligament fractured as the cracks started to overlap with one another, forming ridges on the fractured surfaces.

Bao et al. studied the evolution of pores in AlSi10Mg specimens under tension–tension fatigue testing inside an X-ray micro CT equipment [113]. The results revealed an increase in the pore size and density as the number of cycles progressed. Fatigue testing was performed at room-temperature, as well as high-temperature conditions. Needless to say, it is challenging to build an in-situ thermo-mechanical fatigue testing equipment that can be operated inside a tomography setup. Hence, a fatigue test rig containing a polymethyl methacrylate tube was built that would allow the X-rays to pass through the apparatus and scan the specimens. The high-temperature fatigue experiments showed that the aspect ratio of the pores decreased as the distance increased from the fractured surfaces. The plastic flow lines controlled the length and orientation of the elongation of pores. At high temperatures, a greater reduction in the necking area was observed due to the presence of pores with large aspect ratio. The plastic strain increased with each cycle elongating the pores. The growth rate of the pores was found to depend on the longitudinal strain accumulation both at room and elevated temperatures. The time-lapse images of specimens undergoing fatigue testing at both room and elevated temperatures are shown in Figure 21. In the later stages of the experiments, the pores were found to be tilting because of the shear stress acting on them.

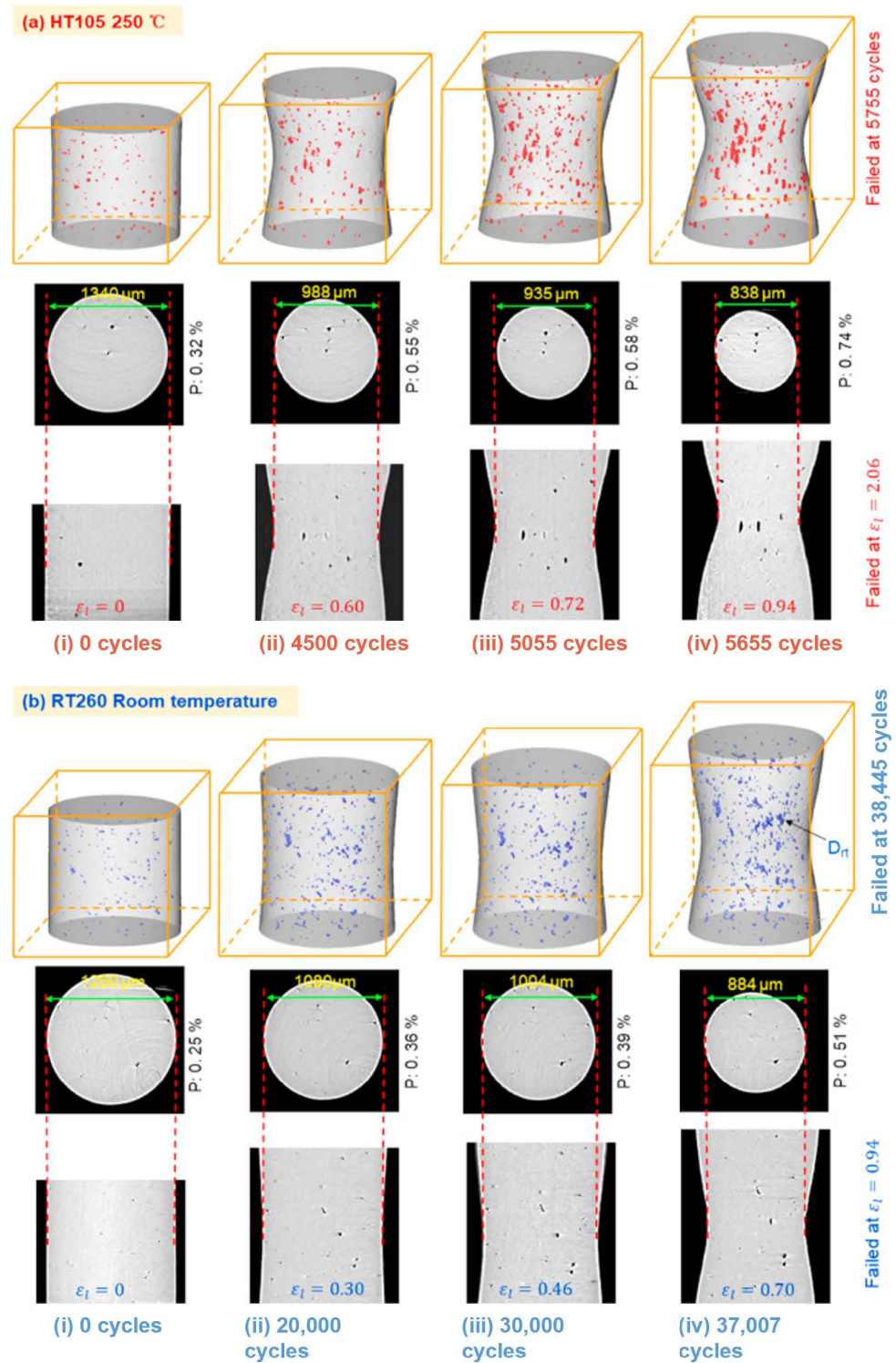


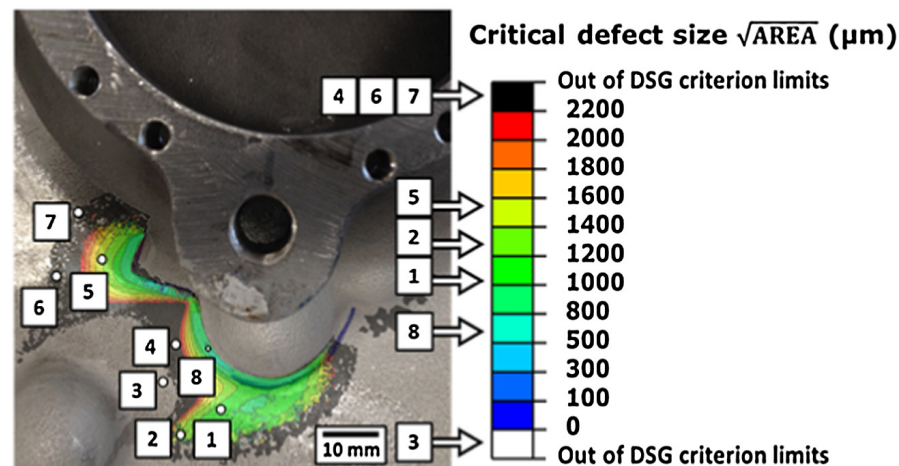
Figure 21. Time-lapse images of (a) the specimen (HT105) tested at 250 °C and peak load of 105 MPa and (b) the specimen (RT260) tested at room temperature test and peak load of 260 MPa as a function of numbers of cycles showing the 3D rendering of the voids (**top**), a virtual mid-plane slice (**middle**), and a diametrical slice (**bottom**) in each case. Reprinted with permission from Ref. [113]. Copyright 2020 Elsevier.

Rhein et al. investigated the crack growth behavior in AlSi10Mg specimens during fatigue testing [114]. Notched specimens were subjected to ultrasonic fatigue testing. X-ray CT scan was simultaneously performed during the testing. CT scans showed that the cracks initiated at the corners of the notches and propagated perpendicular to the loading direction. Bao et al. investigated the impact of internal pores on the fatigue damage accumulation of specimens under tension–tension loading at a high temperature (250 °C) [113]. The damage accumulation and the defect evolution were monitored by synchrotron radiation micro-computed tomography. The pores were found to elongate in the longitudinal direction, and the elongation was 10 times more than that in the lateral direction. The elongation was initially slow, but it increased quickly because of the local longitudinal strain. External deformations were observed for the pores that were closer to the surface of the necking region. The work concluded that under low-cycle fatigue conditions involving high-stress ratios, the growth of the pores in the neck region led to failure. On the contrary, under high-cycle fatigue conditions, the surface pores caused cracking. Wang et al. conducted in-situ SEM investigations of notched AlSi10Mg specimens undergoing fatigue testing at elevated temperatures [115]. The results showed that the failure involved multiple cracks growing simultaneously.

6. Computation Modeling to Predict Fatigue Failure Characteristics

It is estimated that about 90% of engineering failures are related to fatigue [116]. Fatigue testing is a destructive method. Hence, to qualify parts for fatigue-critical applications, a large number of destructive tests are required to be performed to develop predictive correlations. An appreciable amount of cost and time, therefore, needs to be invested. It can be avoided or reduced if there are high-fidelity computational models that can predict the fatigue failure characteristics with high confidence. Nadot et al. employed the ‘defect stress gradient (DSG)’ criterion to predict the influence of pores on the fatigue crack growth [117]. A defect creates a local stress gradient that can be evaluated using DSG. DSG was successful in explaining the influence of defect morphology on fatigue life as well [118,119]. Additionally, DSG was also able to predict the fatigue life under multi-axial loading conditions with different load ratios [120]. The DSG criterion could be applied after performing the finite element analysis to obtain a contour of defect sizes, as shown in Figure 22 [121–123]. Beretta et al. evaluated the fatigue strength as a function of surface pores [35]. The effective stress ratio at the fatigue limit was first evaluated. This limit was then used in obtaining the fatigue strength as a function of surface pores [124]. The work concluded that both residual stress and pore size were important to predict the fatigue properties of a specimen. Gumpinger et al. predicted the fatigue life by using an equivalent initial crack size [125]. The results showed very good predictions with an accuracy of 87% when compared with the experimental data. The ratio between the predicted data and the experimental data varied from 0.5 to 2.

The existing literature shows that fatigue resistance is primarily influenced by the presence of pores [126–128]. Due to the presence of pores, a large scatter in the fatigue test results is typically observed. Murakami et al. showed that the largest part of this scatter could be correlated with the initial pore size, which influenced the lower bound of the fatigue resistance [129]. Romano et al. proposed a model for predicting both fatigue strength and fatigue life. The model was based on the presence of defects, which were treated as cracks [104]. The relationship between the defects and fatigue strength was defined using the modified El-Haddad approach involving the Murakami parameter [127,130–132]. From the model, the best-fit curve was obtained to predict fatigue strength as a function of crack size. To predict the fatigue life of the specimens, crack growth models were also used. The model calculated the stress intensity factors by adopting a simple situation of crack propagation in a rod [133]. Other models, such as elastic simulations considering a plasticity-corrected crack length, were also explored. The latter method proved to be very accurate and useful when the initial crack size was the dominant defect in the specimen.



Artificial defect size 1-7 - $\sqrt{\text{AREA}} = 1250\mu\text{m}$

Artificial defect size 8 - $\sqrt{\text{AREA}} = 945\mu\text{m}$

Figure 22. Defect size map of a specimen. Reprinted with permission from Ref. [121]. Copyright 2017 Elsevier.

Microscale simulations are often required to understand the impact of microstructural inhomogeneity on fatigue strength. Crystal plasticity finite element modeling (CPFEM) can be used to predict the fatigue life of AlSi10Mg specimens undergoing high-cycle and very high-cycle fatigue testing [108,134]. The accumulation of plastic shear strain was found to aggravate around pores and inclusions. These strain accumulations accelerated the crack initiation process reducing the fatigue life. The maximum accumulated plastic strain occurred in the specimens with more pores. Hence, the pores are more problematic than inclusions. The prediction of fatigue life was found to agree with the experimental results in the range of 10^5 to 10^9 cycles. CPFEM was also useful in predicting the behavior of the 3D fatigue crack propagation in the short crack regime [135]. The direction of crack propagation was found to depend on the orientation of the slip systems.

7. Conclusions and Future Research Opportunities

A strong connection exists between the powder properties, printing parameters, post-processing methods, and the fatigue properties of AlSi10Mg specimens. Powders are often reused to minimize the cost of production. Powder reusing leads to a reduction in particle size distribution range as smaller particles agglomerate during the L-PBF process [67]. An increase in the number of reuse cycle causes an increase in the volume fraction of pores lowering the part density [52]. The printing parameters, such as the laser power, scanning speed, hatch spacing, layer thickness, and build orientation, influence the fatigue strength and life of AlSi10Mg specimens. An increase in the layer thickness degrades the fatigue strength [79]. A larger hatch spacing also decreases the fatigue strength. The specimens built along the horizontal direction typically offer higher fatigue strength compared to all other build directions [15]. A lower laser power results in insufficient bonding between the layers, creating lack of fusion pores. A higher laser power causes excessive melting resulting in balling and melt track instability [78].

The fatigue strength of AlSi10Mg specimens can be improved by T6 heat treatment [32,87]. Other unconventional heat treatment procedures, such as HIP + T6 or HP + T6, can also improve the fatigue strength of AlSi10Mg specimens [52,64,91]. Surface treatments, such as shot peening, reduces the surface pores of the specimens. It hardens the surfaces and refines the microstructure, which, in turn, improves the fatigue life of AlSi10Mg specimens [95,100]. Fatigue strength is a function of the loading conditions. Increasing the stress ratio decreases the fatigue strength [108] while increasing the mean stress decreases the

fatigue life [109]. Apart from loading conditions, the presence of notches is also a critical factor. The notched specimens are found to have much lower fatigue strength compared to the un-notched specimens [100]. Numerical models involving El-Haddad approach help to establish correlation between crack geometry and fatigue strength. Crystal plasticity model performs microscale simulation and predicts fatigue life accurately in the range of 10^5 to 10^9 cycles.

The usage of other AM processes, such as DED, is sparse for AlSi10Mg specimens. It is well known that DED is more economical than PBF. Kiani et al. studied the effect of printing parameters on the bulk properties of AlSi10Mg specimen manufactured by laser-DED (L-DED) process [136]. The results showed that the mechanical properties of the specimens were equivalent to that of cast materials. Other than L-PBF and L-DED, electron beam-PBF (EB-PBF) is another AM process that needs to be investigated for AlSi10Mg. The process typically forms a larger melt pool compared to L-PBF, eliminating a significant number of pores and defects [137]. Moreover, the cost of manufacturing is less for EB-PBF than L-PBF if batch production takes place. However, EB-PBF has not gained much attention in processing AlSi10Mg.

The influence of printing parameters on fatigue properties of AlSi10Mg has already been investigated to an appreciable extent. However, the effect of build chamber pressure during the manufacturing of the component is a uncharted territory. Very few works have attempted to investigate the effect of chamber pressure on the microstructures and properties of as-built specimens. Chen et al. investigated the influence of variation of chamber pressure on the microstructure and pores of selectively laser-welded specimens [138]. Low chamber pressure resulted in the formation of large pores. Wu et al. studied the impact of the ambient pressure on powder splashing [139]. A higher pressure was found to increase splashing, which, in turn, increases balling.

Fatigue properties of AlSi10Mg specimens were found to have a lot of scatter even when they were manufactured under identical processing conditions [79]. Hence, it is difficult to develop predictive models for life estimation purposes. An alternate approach could be to use sensors to monitor the fatigue health of specimens in real-time. Dharmadhikari et al. [140] monitored a specimen using a confocal microscope undergoing fatigue tests and calibrated the force-displacement data obtained from a linear variable differential transformer sensor. The authors, thereafter, used a machine-learning algorithm to detect fatigue damages at a crack opening displacement thickness of 10 μm .

AlSi10Mg parts are used in the automobile and aerospace industries. These parts may operate in corrosive environment. It is, therefore, important to conduct research on the corrosion fatigue strength of AM AlSi10Mg specimens. The impact of the printing parameters and powder properties, as well as a variation in the corrosive environment will have to be evaluated. Corrosive environments give rise to pitting attacks on the specimen surfaces. These pitting attacks combined with the porosities result in the formation of many crack initiation sites. Corrosion can also be characterized by the cyclic potentiodynamic polarization analysis as conducted by Leon et al. [101]. In this study, the effect of surface roughness on corrosion fatigue strength of AM AlSi10Mg was investigated. The unpolished specimens had lower strength than the polished specimens because the unpolished specimens had a larger number pores. These pores aggravated the pitting attacks and lowered the fatigue strength of the specimens. Further experiments can be performed inside a computed tomography equipment which will shed critical insights into the crack initiation and propagation behavior in corrosive environment.

Author Contributions: Conceptualization, A.B.; methodology, R.P.; resources, A.B.; writing—original draft preparation, R.P.; writing—review and editing, A.B.; visualization, R.P.; supervision, A.B.; project administration, A.B.; funding acquisition, A.B. All authors have read and agreed to the published version of the manuscript.

Funding: The work reported in this paper was supported in part by the Department of Mechanical Engineering and in part by the Center of Biodevices at the Pennsylvania State University, University Park, PA 16802. The APC was funded by the Alloys Editorial Office.

Data Availability Statement: All data generated or analysed during this study are included in this published article.

Conflicts of Interest: The authors declare no conflict of interest.

Abbreviations

The following abbreviations are used in this manuscript:

AE	Aeration Energy
ASTM	American Society for Testing and Materials
AM	Additive Manufacturing
BFE	Basic Flow Energy
BJ	Binder Jetting
CBD	Conditioned Bulk Density
CFE	Consolidation Flow Energy
CI	Compressibility Index
CPFEM	Crystal Plasticity Finite Element Modeling
CS	Cohesion Stress
CT	Computed Tomography
DED	Directed Energy Deposition
EB-PBF	Electron Beam Powder Bed Fusion
EDS, EDX	Energy Dispersive X-ray Spectroscopy
FESEM	Field Emission Scanning Electron Microscope
HP	High Pressure
HIP	Hot Isostatic Pressing
HCF	High Cycle Fatigue
HT	Heat Treated
LCF	Low cycle Fatigue
L-DED	Laser Directed Energy Deposition
L-PBF	Laser Powder Bed Fusion
OM	Optical Microscopy
PBF	Powder Bed Fusion
SEM	Scanning Electron Microscopy
SE	Specific Energy
SP	Shot Peening
XRD	X-Ray Diffraction

References

1. Raus, A.A.; Wahab, M.S.; Ibrahim, M.; Kamarudin, K.; Ahmed, A.; Shamsudin, S. Mechanical and physical properties of AlSi10Mg processed through selective laser melting. *AIP Conf. Proc.* **2017**, *1831*, 020027. [[CrossRef](#)]
2. Heraeus Additive Manufacturing GmbH. *Metal Powder AlSi10Mg*; Heraeus Additive Manufacturing GmbH: Hanau, Hessen, Germany, 2019; pp. 1–2.
3. EOS Aluminium AlSi10Mg Material Data Sheet EOS Aluminium AlSi10Mg Good Strength & Dynamic Load Bearing Capacity. Available online: https://www.eos.info/03_system-related-assets/material-related-contents/metal-materials-and-examples/metal-material-datasheet/aluminium/material_datasheet_eos_aluminium-alsi10mg_en_web.pdf (accessed on 18 January 2022).
4. Zygula, K.; Nosek, B.; Pasiowicz, H.; Szysiak, N. Mechanical properties and microstructure of AlSi10Mg alloy obtained by casting and SLM technique. *World Sci. News* **2018**, *104*, 456–466.
5. ISO. *Standard Terminology for Additive Manufacturing—General Principles—Terminology*; International Organization for Standardization: Geneva, Switzerland, 2015.

6. Frazier, W.E. Metal additive manufacturing: A review. *J. Mater. Eng. Perform.* **2014**, *23*, 1917–1928. [[CrossRef](#)]
7. Gibson, I.; Rosen, D.; Stucker, B. *Directed Energy Deposition Processes*. In *Additive Manufacturing Technologies*; Springer: New York, NY, USA, 2015; pp. 1–509.
8. Sun, S.; Brandt, M.; Easton, M. *Powder Bed Fusion Processes: An Overview*; Elsevier Ltd.: Amsterdam, The Netherlands, 2017; pp. 55–77. [[CrossRef](#)]
9. Poncelet, O.; Marteleur, M.; van der Rest, C.; Rigo, O.; Adrien, J.; Dancette, S.; Jacques, P.J.; Simar, A. Critical assessment of the impact of process parameters on vertical roughness and hardness of thin walls of AlSi10Mg processed by laser powder bed fusion. *Addit. Manuf.* **2021**, *38*, 101801. [[CrossRef](#)]
10. Gouveia, R.M.; Silva, F.J.G.; Atzeni, E.; Sormaz, D.; Alves, J.L.; Pereira, A.B. Effect of Scan Strategies and Use of Support Structures on Surface Quality and Hardness of L-PBF AlSi10Mg Parts. *Materials* **2020**, *13*, 2248. [[CrossRef](#)]
11. Rafieazad, M.; Fathi, P.; Mohammadi, M.; Nasiri, A. Effects of Laser-Powder Bed Fusion Process Parameters on the Microstructure and Corrosion Properties of AlSi10Mg Alloy. *J. Electrochem. Soc.* **2021**, *168*, 021505. [[CrossRef](#)]
12. Zavala-Arredondo, M.; London, T.; Allen, M.; Maccio, T.; Ward, S.; Griffiths, D.; Allison, A.; Goodwin, P.; Hauser, C. Use of power factor and specific point energy as design parameters in laser powder-bed-fusion (L-PBF) of AlSi10Mg alloy. *Mater. Des.* **2019**, *182*, 108018. [[CrossRef](#)]
13. Salmi, A.; Atzeni, E. Residual stress analysis of thin AlSi10Mg parts produced by Laser Powder Bed Fusion. *Virtual Phys. Prototyp.* **2020**, *15*, 49–61. [[CrossRef](#)]
14. Salmi, A.; Piscopo, G.; Atzeni, E.; Minetola, P.; Iuliano, L. On the Effect of Part Orientation on Stress Distribution in AlSi10Mg Specimens Fabricated by Laser Powder Bed Fusion (L-PBF). *Procedia CIRP* **2018**, *67*, 191–196. [[CrossRef](#)]
15. Brandl, E.; Heckenberger, U.; Holzinger, V.; Buchbinder, D. Additive manufactured AlSi10Mg samples using Selective Laser Melting (SLM): Microstructure, high cycle fatigue, and fracture behavior. *Mater. Des.* **2012**, *34*, 159–169. [[CrossRef](#)]
16. Wang, T.; Wang, Y.; Chen, C.; Zhu, H. Relationships between the characteristics of porosity, melt pool and process parameters in laser powder bed fusion AlZn alloy. *J. Manuf. Process.* **2021**, *68*, 1236–1244. [[CrossRef](#)]
17. Giovagnoli, M.; Silvi, G.; Merlin, M.; Di Giovanni, M.T. Optimisation of process parameters for an additively manufactured AlSi10Mg alloy: Limitations of the energy density-based approach on porosity and mechanical properties estimation. *Mater. Sci. Eng. A* **2021**, *802*, 140613. [[CrossRef](#)]
18. Maurya, N.K.; Srivastava, A.K.; Saxena, A.; Dwivedi, S.P.; Ashraf Ali, M.; Mustafa, J. Experimental investigation on the effect of laser powder bed fusion process variables on dimensional accuracy, surface roughness and cylindricity of the AlSi10Mg alloy component. *Proc. Inst. Mech. Eng. Part J. Process Mech. Eng.* **2021**, 09544089211039046. [[CrossRef](#)]
19. Calignano, F. Investigation of the accuracy and roughness in the laser powder bed fusion process. *Virtual Phys. Prototyp.* **2018**, *13*, 97–104. [[CrossRef](#)]
20. Hadadzadeh, A.; Amirkhiz, B.S.; Langelier, B.; Li, J.; Mohammadi, M. Microstructural consistency in the additive manufactured metallic materials: A study on the laser powder bed fusion of AlSi10Mg. *Addit. Manuf.* **2021**, *46*, 102166. [[CrossRef](#)]
21. Albu, M.; Krisper, R.; Lammer, J.; Kothleitner, G.; Fiochi, J.; Bassani, P. Microstructure evolution during in-situ heating of AlSi10Mg alloy powders and additive manufactured parts. *Addit. Manuf.* **2020**, *36*, 101605. doi: 10.1016/j.addma.2020.101605. [[CrossRef](#)]
22. Torino, P. Influence of the Laser Beam Focus on the Mechanical Properties and Microstructure of AlSi10Mg Processed by L-PBF. 2021. Available online: <https://webthesis.biblio.polito.it/20200/1/tesi.pdf> (accessed on 18 January 2022).
23. Silvestri, A.T.; Astarita, A.; Hassanin, A.E.; Manzo, A.; Iannuzzo, U.; Iannuzzo, G.; de Rosa, V.; Acerra, F.; Squillace, A. Assessment of the mechanical properties of AlSi10Mg parts produced through selective laser melting under different conditions. *Procedia Manuf.* **2020**, *47*, 1058–1064. [[CrossRef](#)]
24. Park, T.H.; Baek, M.S.; Hyer, H.; Sohn, Y.; Lee, K.A. Effect of direct aging on the microstructure and tensile properties of AlSi10Mg alloy manufactured by selective laser melting process. *Mater. Charact.* **2021**, *176*, 111113. [[CrossRef](#)]
25. Ponticelli, G.S.; Giannini, O.; Guarino, S.; Horn, M. An optimal fuzzy decision-making approach for laser powder bed fusion of AlSi10Mg alloy. *J. Manuf. Process.* **2020**, *58*, 712–723. [[CrossRef](#)]
26. Kusoglu, I.M.; Gökce, B.; Barcikowski, S. Research trends in laser powder bed fusion of Al alloys within the last decade. *Addit. Manuf.* **2020**, *36*, 101489. [[CrossRef](#)]
27. Balbaa, M.A.; Ghasemi, A.; Fereiduni, E.; Elbestawi, M.A.; Jadhav, S.D.; Kruth, J.P. Role of powder particle size on laser powder bed fusion processability of AlSi10Mg alloy. *Addit. Manuf.* **2021**, *37*, 101630. [[CrossRef](#)]
28. Kumar, M.S.; Javidrad, H.R.; Shanmugam, R.; Ramoni, M.; Adedirani, A.A.; Pruncu, C.I. Impact of Print Orientation on Morphological and Mechanical Properties of L-PBF Based AlSi7Mg Parts for Aerospace Applications. *Silicon* **2021**. [[CrossRef](#)]
29. Rafieazad, M.; Mohammadi, M.; Gerlich, A.; Nasiri, A. Enhancing the corrosion properties of additively manufactured AlSi10Mg using friction stir processing. *Corros. Sci.* **2021**, *178*, 109073. [[CrossRef](#)]
30. Ghasemi, A.; Fereiduni, E.; Balbaa, M.; Jadhav, S.D.; Elbestawi, M.; Habibi, S. Influence of alloying elements on laser powder bed fusion processability of aluminum: A new insight into the oxidation tendency. *Addit. Manuf.* **2021**, *46*, 102145. [[CrossRef](#)]

31. Tang, M. Inclusions, Porosity, and Fatigue of AlSi10Mg Parts Produced by Selective Laser Melting. Ph.D. Dissertation, Carnegie Mellon University, Pittsburgh, PA, USA, 2017; p. 184.
32. Aboulkhair, N.T.; Maskery, I.; Tuck, C.; Ashcroft, I.; Everitt, N.M. The microstructure and mechanical properties of selectively laser melted AlSi10Mg: The effect of a conventional T6-like heat treatment. *Mater. Sci. Eng. A* **2016**, *667*, 139–146. [CrossRef]
33. Bagherifard, S.; Beretta, N.; Monti, S.; Riccio, M.; Bandini, M.; Guagliano, M. On the fatigue strength enhancement of additive manufactured AlSi10Mg parts by mechanical and thermal post-processing. *Mater. Des.* **2018**, *145*, 28–41. [CrossRef]
34. Hadadzadeh, A.; Baxter, C.; Amirkhiz, B.S.; Mohammadi, M. Strengthening mechanisms in direct metal laser sintered AlSi10Mg: Comparison between virgin and recycled powders. *Addit. Manuf.* **2018**, *23*, 108–120. [CrossRef]
35. Beretta, S.; Gargourimotlagh, M.; Foletti, S.; du Plessis, A.; Riccio, M. Fatigue strength assessment of “as built” AlSi10Mg manufactured by SLM with different build orientations. *Int. J. Fatigue* **2020**, *139*, 105737. [CrossRef]
36. Moghimian, P.; Poirié, T.; Habibnejad-Korayem, M.; Zavala, J.A.; Kroeger, J.; Marion, F.; Larouche, F. Metal powders in additive manufacturing: A review on reusability and recyclability of common titanium, nickel and aluminum alloys. *Addit. Manuf.* **2021**, *43*, 102017. [CrossRef]
37. Brika, S.E.; Letenneur, M.; Dion, C.A.; Brailovski, V. Influence of particle morphology and size distribution on the powder flowability and laser powder bed fusion manufacturability of Ti-6Al-4V alloy. *Addit. Manuf.* **2020**, *31*, 100929. [CrossRef]
38. Zhao, Y.; Cui, Y.; Hasebe, Y.; Bian, H.; Yamanaka, K.; Aoyagi, K.; Hagisawa, T.; Chiba, A. Controlling factors determining flowability of powders for additive manufacturing: A combined experimental and simulation study. *Powder Technol.* **2021**, *393*, 482–493. [CrossRef]
39. Gao, C.F.; Xiao, Z.Y.; Zou, H.P.; Liu, Z.Q.; Jin, C.; Li, S.K.; Zhang, D.T. Characterization of spherical AlSi10Mg powder produced by double-nozzle gas atomization using different parameters. *Trans. Nonferrous Met. Soc. China* **2019**, *29*, 374–384. [CrossRef]
40. Achelis, L.; Uhlenwinkel, V. Characterisation of metal powders generated by a pressure-gas-atomiser. *Mater. Sci. Eng. A* **2008**, *477*, 15–20. [CrossRef]
41. Metz, R.; Machado, C.; Houabes, M.; Pansiot, J.; Elkhatib, M.; Puyanē, R.; Hassanzadeh, M. Nitrogen spray atomization of molten tin metal: Powder morphology characteristics. *J. Mater. Process. Technol.* **2007**, *189*, 132–137. [CrossRef]
42. Aksoy, A.; Ünal, R. Effects of gas pressure and protrusion length of melt delivery tube on powder size and powder morphology of nitrogen gas atomised tin powders. *Powder Metall.* **2006**, *49*, 349–354. [CrossRef]
43. gang Li, X.; Zhu, Q.; Shu, S.; zhong Fan, J.; ming Zhang, S. Fine spherical powder production during gas atomization of pressurized melts through melt nozzles with a small inner diameter. *Powder Technol.* **2019**, *356*, 759–768. [CrossRef]
44. Material Data Sheet SLM Solutions Group Ag. Available online: https://www.slm-solutions.com/fileadmin/Content/Powder/MDS/MDS_Al-Alloy_AlSi10Mg_0221.pdf (accessed on 18 January 2022).
45. Riener, K.; Albrecht, N.; Ziegelmeier, S.; Ramakrishnan, R.; Haferkamp, L.; Spierings, A.B.; Leichtfried, G.J. Influence of particle size distribution and morphology on the properties of the powder feedstock as well as of AlSi10Mg parts produced by laser powder bed fusion (LPBF). *Addit. Manuf.* **2020**, *34*, 101286. [CrossRef]
46. Hausner, H.H. *Friction Conditions in a Mass of Metal Powder*; Technical Report; Polytechnic Institute of Brooklyn, University of California: Los Angeles, CA, USA, 1967.
47. Chu, F.; Zhang, K.; Shen, H.; Liu, M.; Huang, W.; Zhang, X.; Liang, E.; Zhou, Z.; Lei, L.; Hou, J.; et al. Influence of satellite and agglomeration of powder on the processability of AlSi10Mg powder in Laser Powder Bed Fusion. *J. Mater. Res. Technol.* **2021**, *11*, 2059–2073. [CrossRef]
48. Freeman, R. Measuring the flow properties of consolidated, conditioned and aerated powders—A comparative study using a powder rheometer and a rotational shear cell. *Powder Technol.* **2007**, *174*, 25–33. [CrossRef]
49. Freeman, R.; Fu, X. Characterisation of power bulk, dynamic flow and shear properties in relation to die filling. *Powder Metall.* **2008**, *51*, 196–201. [CrossRef]
50. Forte, G.; Clark, P.J.; Yan, Z.; Stitt, E.H.; Marigo, M. Using a Freeman FT4 rheometer and Electrical Capacitance Tomography to assess powder blending. *Powder Technol.* **2018**, *337*, 25–35. [CrossRef]
51. Weiss, C.; Munk, J.; Haefner, C.L. Investigation Towards AlSi10Mg Powder Recycling Behavior in the LPBF Process and Its Influences on Mechanical Properties. In *Solid Freeform Fabrication 2016: Proceedings of the 26th Annual International Solid Freeform Fabrication Symposium—An Additive Manufacturing Conference Reviewed Paper*; University of Texas at Austin: Austin, TX, USA, 2016; pp. 2271–2281.
52. Tradowsky, U.; White, J.; Ward, R.M.; Read, N.; Reimers, W.; Attallah, M.M. Selective laser melting of AlSi10Mg: Influence of post-processing on the microstructural and tensile properties development. *Mater. Des.* **2016**, *105*, 212–222. [CrossRef]
53. Wei, P.; Wei, Z.; Chen, Z.; Du, J.; He, Y.; Li, J.; Zhou, Y. The AlSi10Mg samples produced by selective laser melting: Single track, densification, microstructure and mechanical behavior. *Appl. Surf. Sci.* **2017**, *408*, 38–50. [CrossRef]
54. Dai, D.; Gu, D. Effect of metal vaporization behavior on keyhole-mode surface morphology of selective laser melted composites using different protective atmospheres. *Appl. Surf. Sci.* **2015**, *355*, 310–319. [CrossRef]
55. Yadroitsev, I.; Gusarov, A.; Yadroitsava, I.; Smurov, I. Single track formation in selective laser melting of metal powders. *J. Mater. Process. Technol.* **2010**, *210*, 1624–1631. [CrossRef]
56. Kang, N.; Coddet, P.; Liao, H.; Coddet, C. Macroseggregation mechanism of primary silicon phase in selective laser melting hypereutectic Al - High Si alloy. *J. Alloys Compd.* **2016**, *662*, 259–262. [CrossRef]

57. Kang, N.; Coddet, P.; Dembinski, L.; Liao, H.; Coddet, C. Microstructure and strength analysis of eutectic Al-Si alloy in-situ manufactured using selective laser melting from elemental powder mixture. *J. Alloys Compd.* **2017**, *691*, 316–322. [CrossRef]
58. Zhou, L.; Mehta, A.; Schulz, E.; McWilliams, B.; Cho, K.; Sohn, Y. Microstructure, precipitates and hardness of selectively laser melted AlSi10Mg alloy before and after heat treatment. *Mater. Charact.* **2018**, *143*, 5–17. [CrossRef]
59. Fite, J.; Eswarappa Prameela, S.; Slotwinski, J.A.; Weihs, T.P. Evolution of the microstructure and mechanical properties of additively manufactured AlSi10Mg during room temperature holds and low temperature aging. *Addit. Manuf.* **2020**, *36*, 101429. [CrossRef]
60. Takata, N.; Kodaira, H.; Sekizawa, K.; Suzuki, A.; Kobashi, M. Change in microstructure of selectively laser melted AlSi10Mg alloy with heat treatments. *Mater. Sci. Eng. A* **2017**, *704*, 218–228. [CrossRef]
61. Herzog, D.; Seyda, V.; Wycisk, E.; Emmelmann, C. Additive manufacturing of metals. *Acta Mater.* **2016**, *117*, 371–392. [CrossRef]
62. Thijs, L.; Kempen, K.; Kruth, J.P.; Van Humbeeck, J. Fine-structured aluminium products with controllable texture by selective laser melting of pre-alloyed AlSi10Mg powder. *Acta Mater.* **2013**, *61*, 1809–1819. [CrossRef]
63. Holesinger, T.G.; Carpenter, J.S.; Lienert, T.J.; Patterson, B.M.; Papin, P.A.; Swenson, H.; Cordes, N.L. Characterization of an Aluminum Alloy Hemispherical Shell Fabricated via Direct Metal Laser Melting. *JOM* **2016**, *68*, 1000–1011. [CrossRef]
64. Tocci, M.; Pola, A.; Gelfi, M.; La Vecchia, G.M. Effect of a New High-Pressure Heat Treatment on Additively Manufactured AlSi10Mg Alloy. *Metall. Mater. Trans. A Phys. Metall. Mater. Sci.* **2020**, *51*, 4799–4811. [CrossRef]
65. Simpson, T.W. Why Does My 3D-Printed Part Cost So Much? 2018. Available online: <https://www.additivemanufacturing.media/articles/why-does-my-3d-printed-part-cost-so-much> (accessed on 18 January 2022).
66. Recycled Powder Use Is Cost-Effective for Additive Manufacturing. 2018. Available online: <https://www.laserfocusworld.com/industrial-laser-solutions/article/14220902/recycled-powder-use-is-costeffective-for-additive-manufacturing> (accessed on 18 January 2022).
67. Del Re, F.; Contaldi, V.; Astarita, A.; Palumbo, B.; Squillace, A.; Corrado, P.; Di Petta, P. Statistical approach for assessing the effect of powder reuse on the final quality of AlSi10Mg parts produced by laser powder bed fusion additive manufacturing. *Int. J. Adv. Manuf. Technol.* **2018**, *97*, 2231–2240. [CrossRef]
68. Skallerud, B.; Iveland, T.; Härkegård, G. Fatigue life assessment of aluminum alloys with casting defects. *Eng. Fract. Mech.* **1993**, *44*, 857–874. [CrossRef]
69. Hu, Y.N.; Wu, S.C.; Withers, P.J.; Zhang, J.; Bao, H.Y.; Fu, Y.N.; Kang, G.Z. The effect of manufacturing defects on the fatigue life of selective laser melted Ti-6Al-4V structures. *Mater. Des.* **2020**, *192*. [CrossRef]
70. Sonsino, C.M.; Ziese, J. Fatigue strength and applications of cast aluminium alloys with different degrees of porosity. *Int. J. Fatigue* **1993**, *15*, 75–84. [CrossRef]
71. Ferro, P.; Fabrizi, A.; Berto, F.; Savio, G.; Meneghello, R.; Rosso, S. Defects as a root cause of fatigue weakening of additively manufactured AlSi10Mg components. *Theor. Appl. Fract. Mech.* **2020**, *108*, 102611. [CrossRef]
72. Laursen, C.M.; DeJong, S.A.; Dickens, S.M.; Exil, A.N.; Susan, D.F.; Carroll, J.D. Relationship between ductility and the porosity of additively manufactured AlSi10Mg. *Mater. Sci. Eng. A* **2020**, *795*, 139922. [CrossRef]
73. Susan, D.; Crenshaw, T.; Gearhart, J. The effects of casting porosity on the tensile behavior of investment cast 17-4PH stainless steel. *J. Mater. Eng. Perform.* **2015**, *24*, 2917–2924. [CrossRef]
74. Caceres, C.; Selling, B. Casting defects and the tensile properties of an AlSiMg alloy. *Mater. Sci. Eng. A* **1996**, *220*, 109–116. [CrossRef]
75. Narasimharaju, S.R.; Zeng, W.; See, T.L.; Zhu, Z.; Scott, P.; Jiang, X.; Lou, S. A comprehensive review on laser powder bed fusion of steels: Processing, microstructure, defects and control methods, mechanical properties, current challenges and future trends. *J. Manuf. Process.* **2022**, *75*, 375–414. [CrossRef]
76. Simchi, A. Direct laser sintering of metal powders: Mechanism, kinetics and microstructural features. *Mater. Sci. Eng. A* **2006**, *428*, 148–158. [CrossRef]
77. Calignano, F.; Manfredi, D.; Ambrosio, E.P.; Iuliano, L.; Fino, P. Influence of process parameters on surface roughness of aluminum parts produced by DMLS. *Int. J. Adv. Manuf. Technol.* **2013**, *67*, 2743–2751. [CrossRef]
78. Olakanmi, E.O. Selective laser sintering/melting (SLS/SLM) of pure Al, Al-Mg, and Al-Si powders: Effect of processing conditions and powder properties. *J. Mater. Process. Technol.* **2013**, *213*, 1387–1405. [CrossRef]
79. Brandão, A.D.; Gumpinger, J.; Gschweidl, M.; Seyfert, C.; Hofbauer, P.; Ghidini, T. Fatigue Properties of Additively Manufactured AlSi10Mg—Surface Treatment Effect. *Procedia Struct. Integr.* **2017**, *7*, 58–66. [CrossRef]
80. Tang, M.; Pistorius, P.C. Anisotropic Mechanical Behavior of AlSi10Mg Parts Produced by Selective Laser Melting. *JOM* **2017**, *69*, 516–522. [CrossRef]
81. Zimmermann, M.; Müller, D.; Kirsch, B.; Greco, S.; Aurich, J.C. Analysis of the machinability when milling AlSi10Mg additively manufactured via laser-based powder bed fusion. *Int. J. Adv. Manuf. Technol.* **2021**, *112*, 989–1005. [CrossRef]
82. Beevers, E.; Brandão, A.D.; Gumpinger, J.; Gschweidl, M.; Seyfert, C.; Hofbauer, P.; Rohr, T.; Ghidini, T. Fatigue properties and material characteristics of additively manufactured AlSi10Mg—Effect of the contour parameter on the microstructure, density, residual stress, roughness and mechanical properties. *Int. J. Fatigue* **2018**, *117*, 148–162. [CrossRef]
83. Sujakhu, S.; Castagne, S.; Sakaguchi, M.; Kasvayee, K.A.; Ghassemali, E.; Jarfors, A.E.; Wang, W. On the fatigue damage micromechanisms in Si-solution-strengthened spheroidal graphite cast iron. *Fatigue Fract. Eng. Mater. Struct.* **2018**, *41*, 625–641. [CrossRef]

84. Del Re, F.; Scherillo, F.; Contaldi, V.; Palumbo, B.; Squillace, A.; Corrado, P.; Di Petta, P. Mechanical properties characterisation of AlSi10Mg parts produced by laser powder bed fusion additive manufacturing. *Int. J. Mater. Res.* **2019**, *110*, 436–446. [[CrossRef](#)]
85. Rosenthal, I.; Stern, A.; Frage, N. Microstructure and Mechanical Properties of AlSi10Mg Parts Produced by the Laser Beam Additive Manufacturing (AM) Technology. *Metallogr. Microstruct. Anal.* **2014**, *3*, 448–453. [[CrossRef](#)]
86. Kempen, K.; Thijs, L.; Van Humbeeck, J.; Kruth, J.P. Mechanical Properties of AlSi10Mg Produced by Selective Laser Melting. *Phys. Procedia* **2012**, *39*, 439–446. [[CrossRef](#)]
87. Aboulkhair, N.T.; Maskery, I.; Tuck, C.; Ashcroft, I.; Everitt, N.M. Improving the fatigue behaviour of a selectively laser melted aluminium alloy: Influence of heat treatment and surface quality. *Mater. Des.* **2016**, *104*, 174–182. [[CrossRef](#)]
88. Aboulkhair, N.T.; Tuck, C.; Ashcroft, I.; Maskery, I.; Everitt, N.M. On the precipitation hardening of selective laser melted AlSi10Mg. *Metall. Mater. Trans. A* **2015**, *46*, 3337–3341. [[CrossRef](#)]
89. Kempf, A.; Hilgenberg, K. Influence of heat treatments on AlSi10Mg specimens manufactured with different laser powder bed fusion machines. *Mater. Sci. Eng. A* **2021**, *818*, 141371. [[CrossRef](#)]
90. Kan, W.H.; Nadot, Y.; Foley, M.; Ridosz, L.; Proust, G.; Cairney, J.M. Factors that affect the properties of additively-manufactured AlSi10Mg: Porosity versus microstructure. *Addit. Manuf.* **2019**, *29*, 100805. [[CrossRef](#)]
91. Girelli, L.; Tocci, M.; Gelfi, M.; Pola, A. Study of heat treatment parameters for additively manufactured AlSi10Mg in comparison with corresponding cast alloy. *Mater. Sci. Eng. A* **2019**, *739*, 317–328. [[CrossRef](#)]
92. Maamoun, A.H.; Elbestawi, M.; Dosbaeva, G.K.; Veldhuis, S.C. Thermal post-processing of AlSi10Mg parts produced by Selective Laser Melting using recycled powder. *Addit. Manuf.* **2018**, *21*, 234–247. [[CrossRef](#)]
93. Tammam-Williams, S.; Withers, P.J.; Todd, I.; Prangnell, P.B. Porosity regrowth during heat treatment of hot isostatically pressed additively manufactured titanium components. *Scr. Mater.* **2016**, *122*, 72–76. [[CrossRef](#)]
94. Eisaabadi B., G.; Yeom, G.Y.; Tiryakioğlu, M.; Netto, N.; Beygi, R.; Mehrizi, M.Z.; Kim, S.K. The effect of solution treatment time on the microstructure and ductility of naturally-aged A383 alloy die castings. *Mater. Sci. Eng. A* **2018**, *722*, 1–7. [[CrossRef](#)]
95. Uzan, N.E.; Shneck, R.; Yeheskel, O.; Frage, N. Fatigue of AlSi10Mg specimens fabricated by additive manufacturing selective laser melting (AM-SLM). *Mater. Sci. Eng. A* **2017**, *704*, 229–237. [[CrossRef](#)]
96. Schneller, W.; Leitner, M.; Springer, S.; Grün, F.; Taschauer, M. Effect of hip treatment on microstructure and fatigue strength of selectively laser melted AlSi10Mg. *J. Manuf. Mater. Process.* **2019**, *3*, 16. [[CrossRef](#)]
97. Maskery, I.; Aboulkhair, N.T.; Tuck, C.; Wildman, R.D.; Ashcroft, I.A.; Everitt, N.M.; Hague, R.J. Fatigue performance enhancement of selectively laser melted aluminium alloy by heat treatment. In Proceedings of the 26th Annual International Solid Freeform Fabrication Symposium—An Additive Manufacturing Conference, Austin, TX, USA, 10–12 August 2015, pp. 1017–1025.
98. Majzoobi, G.H.; Azizi, R.; Alavi Nia, A. A three-dimensional simulation of shot peening process using multiple shot impacts. *J. Mater. Process. Technol.* **2005**, *164–165*, 1226–1234. [[CrossRef](#)]
99. Maamoun, A.H.; Elbestawi, M.A.; Veldhuis, S.C. Influence of shot peening on alsi10mg parts fabricated by additive manufacturing. *J. Manuf. Mater. Process.* **2018**, *2*, 40. [[CrossRef](#)]
100. Maleki, E.; Bagherifard, S.; Razavi, S.M.J.; Riccio, M.; Bandini, M.; du Plessis, A.; Berto, F.; Guagliano, M. Fatigue behaviour of notched laser powder bed fusion AlSi10Mg after thermal and mechanical surface post-processing. *Mater. Sci. Eng. A* **2022**, *829*, 142145. [[CrossRef](#)]
101. Leon, A.; Aghion, E. Effect of surface roughness on corrosion fatigue performance of AlSi10Mg alloy produced by Selective Laser Melting (SLM). *Mater. Charact.* **2017**, *131*, 188–194. [[CrossRef](#)]
102. Maleki, E.; Bagherifard, S.; Unal, O.; Bandini, M.; Guagliano, M. On the effects of laser shock peening on fatigue behavior of V-notched AlSi10Mg manufactured by laser powder bed fusion. *Int. J. Fatigue* **2022**, *163*, 107035. [[CrossRef](#)]
103. Awd, M.; Siddique, S.; Johannsen, J.; Emmelmann, C.; Walther, F. Very high-cycle fatigue properties and microstructural damage mechanisms of selective laser melted AlSi10Mg alloy. *Int. J. Fatigue* **2019**, *124*, 55–69. [[CrossRef](#)]
104. Romano, S.; Patriarca, L.; Foletti, S.; Beretta, S. LCF behaviour and a comprehensive life prediction model for AlSi10Mg obtained by SLM. *Int. J. Fatigue* **2018**, *117*, 47–62. [[CrossRef](#)]
105. Romano, S.; Brückner-Foit, A.; Brandão, A.; Gumpinger, J.; Ghidini, T.; Beretta, S. Fatigue properties of AlSi10Mg obtained by additive manufacturing: Defect-based modelling and prediction of fatigue strength. *Eng. Fract. Mech.* **2018**, *187*, 165–189. [[CrossRef](#)]
106. Shamsaei, N.; Yadollahi, A.; Bian, L.; Thompson, S.M. An overview of Direct Laser Deposition for additive manufacturing; Part II: Mechanical behavior, process parameter optimization and control. *Addit. Manuf.* **2015**, *8*, 12–35. [[CrossRef](#)]
107. Buffière, J.Y.; Savelli, S.; Jouneau, P.H.; Maire, E.; Fougères, R. Experimental study of porosity and its relation to fatigue mechanisms of model Al-Si7-MgO.3 cast Al alloys. *Mater. Sci. Eng. A* **2001**, *316*, 115–126. [[CrossRef](#)]
108. Zhang, J.; Li, J.; Wu, S.; Zhang, W.; Sun, J.; Qian, G. High-cycle and very-high-cycle fatigue lifetime prediction of additively manufactured AlSi10Mg via crystal plasticity finite element method. *Int. J. Fatigue* **2022**, *155*, 106577. [[CrossRef](#)]
109. Qian, G.; Jian, Z.; Qian, Y.; Pan, X.; Ma, X.; Hong, Y. Very-high-cycle fatigue behavior of AlSi10Mg manufactured by selective laser melting: Effect of build orientation and mean stress. *Int. J. Fatigue* **2020**, *138*, 105696. [[CrossRef](#)]

110. Tridello, A.; Biffi, C.A.; Fiocchi, J.; Bassani, P.; Chiandussi, G.; Rossetto, M.; Tuissi, A.; Paolino, D.S. VHCF response of as-built SLM AlSi10Mg specimens with large loaded volume. *Fatigue Fract. Eng. Mater. Struct.* **2018**, *41*, 1918–1928. [[CrossRef](#)]
111. Nicoletto, G. Influence of rough as-built surfaces on smooth and notched fatigue behavior of L-PBF AlSi10Mg. *Addit. Manuf.* **2020**, *34*, 101251. [[CrossRef](#)]
112. Qian, W.; Wu, S.; Wu, Z.; Ahmed, S.; Zhang, W.; Qian, G.; Withers, P.J. In situ X-ray imaging of fatigue crack growth from multiple defects in additively manufactured AlSi10Mg alloy. *Int. J. Fatigue* **2022**, *155*, 106616. [[CrossRef](#)]
113. Bao, J.; Wu, S.; Withers, P.J.; Wu, Z.; Li, F.; Fu, Y.; Sun, W. Defect evolution during high temperature tension-tension fatigue of SLM AlSi10Mg alloy by synchrotron tomography. *Mater. Sci. Eng. A* **2020**, *792*, 139809. [[CrossRef](#)]
114. Rhein, R.K.; Shi, Q.; Tekalur, S.A.; Jones, J.W.; Carroll, J.W. Short-Crack Growth Behavior in Additively Manufactured AlSi10Mg Alloy. *J. Mater. Eng. Perform.* **2021**, *30*, 5392–5398. [[CrossRef](#)]
115. Wang, Z.; Wu, W.; Qian, G.; Sun, L.; Li, X.; Correia, J.A. In-situ SEM investigation on fatigue behaviors of additive manufactured Al-Si10-Mg alloy at elevated temperature. *Eng. Fract. Mech.* **2019**, *214*, 149–163. [[CrossRef](#)]
116. Zhang, C.; Zhu, H.; Liao, H.; Cheng, Y.; Hu, Z.; Zeng, X. Effect of heat treatments on fatigue property of selective laser melting AlSi10Mg. *Int. J. Fatigue* **2018**, *116*, 513–522. [[CrossRef](#)]
117. Nadot, Y.; Nadot-Martin, C.; Kan, W.H.; Boufadene, S.; Foley, M.; Cairney, J.; Proust, G.; Ridosz, L. Predicting the fatigue life of an AlSi10Mg alloy manufactured via laser powder bed fusion by using data from computed tomography. *Addit. Manuf.* **2020**, *32*, 100899. [[CrossRef](#)]
118. Billaudeau, T.; Nadot, Y.; Bezine, G. Multiaxial fatigue limit for defective materials: Mechanisms and experiments. *Acta Mater.* **2004**, *52*, 3911–3920. [[CrossRef](#)]
119. Nadot, Y.; Billaudeau, T. Multiaxial fatigue limit criterion for defective materials. *Eng. Fract. Mech.* **2006**, *73*, 112–133. [[CrossRef](#)]
120. Gadouini, H.; Nadot, Y.; Rebours, C. Influence of mean stress on the multiaxial fatigue behaviour of defective materials. *Int. J. Fatigue* **2008**, *30*, 1623–1633. [[CrossRef](#)]
121. Rotella, A.; Nadot, Y.; Augustin, R.; Piellard, M.; L’Heritier, S. Defect size map for cast A357-T6 component under multiaxial fatigue loading using the Defect Stress Gradient (DSG) criterion. *Eng. Fract. Mech.* **2017**, *174*, 227–242. [[CrossRef](#)]
122. Mura, T. Mechanics of elastic and inelastic solids. In *Micromechanics of Defects in Solids*; Martinus Nijhoff Publishers: Dordrecht, The Netherlands, 1987.
123. Eshelby, J. Elastic inclusions and inhomogeneities. *Prog. Solid Mech.* **1961**, *2*, 89–140.
124. Kitagawa, H. Applicability of fracture mechanics to very small cracks or the cracks in the early stage. In Proceedings of the 2nd ICM, Cleveland, OH, USA, 16–24 August 1976; Volume 1976, pp. 627–631.
125. Gumpinger, J.; Brandão, A.D.; Beevers, E.; Rohr, T.; Ghidini, T.; Beretta, S.; Romano, S. *Expression of Additive Manufacturing Surface Irregularities through a Flaw-Based Assessment*; ASTM Special Technical Publication; STP 1620; ASTM International: West Conshohocken, PA, USA, 2020; pp. 234–249. [[CrossRef](#)]
126. Yadollahi, A.; Shamsaei, N. Additive manufacturing of fatigue resistant materials: Challenges and opportunities. *Int. J. Fatigue* **2017**, *98*, 14–31. [[CrossRef](#)]
127. Beretta, S.; Romano, S. A comparison of fatigue strength sensitivity to defects for materials manufactured by AM or traditional processes. *Int. J. Fatigue* **2017**, *94*, 178–191. [[CrossRef](#)]
128. Leuders, S.; Thöne, M.; Riemer, A.; Niendorf, T.; Tröster, T.; Richard, H.A.; Maier, H.J. On the mechanical behaviour of titanium alloy TiAl6V4 manufactured by selective laser melting: Fatigue resistance and crack growth performance. *Int. J. Fatigue* **2013**, *48*, 300–307. [[CrossRef](#)]
129. Murakami, Y. *Metal Fatigue: Effects of Small Defects and Nonmetallic Inclusions*; Academic Press: Cambridge, MA, USA, 2019.
130. Beretta, S.; Carboni, M.; Madia, M. Modelling of fatigue thresholds for small cracks in a mild steel by “Strip-Yield” model. *Eng. Fract. Mech.* **2009**, *76*, 1548–1561. [[CrossRef](#)]
131. El Haddad, M.; Topper, T.; Smith, K. Prediction of non propagating cracks. *Eng. Fract. Mech.* **1979**, *11*, 573–584. [[CrossRef](#)]
132. Murakami, Y.; Endo, M. Effects of hardness and crack geometries on delta k sub th of small cracks emanating from small defects. In *The Behaviour of Short Fatigue Cracks*; Mechanical Engineering Publications: Suffolk, UK, 1986; pp. 275–293.
133. Forman, R.; Shivakumar, V. Growth behavior of surface cracks in the circumferential plane of solid and hollow cylinders. In *Fracture Mechanics: Seventeenth Volume*; ASTM International: West Conshohocken, PA, USA, 1986.
134. Zhang, W.; Hu, Y.; Ma, X.; Qian, G.; Zhang, J.; Yang, Z.; Berto, F. Very-high-cycle fatigue behavior of AlSi10Mg manufactured by selected laser melting: Crystal plasticity modeling. *Int. J. Fatigue* **2021**, *145*, 106109. [[CrossRef](#)]
135. Proudhon, H.; Li, J.; Wang, F.; Roos, A.; Chiaruttini, V.; Forest, S. 3D simulation of short fatigue crack propagation by finite element crystal plasticity and remeshing. *Int. J. Fatigue* **2016**, *82*, 238–246. [[CrossRef](#)]
136. Kiani, P.; Dupuy, A.D.; Ma, K.; Schoenung, J.M. Directed energy deposition of AlSi10Mg: Single track nonscalability and bulk properties. *Mater. Des.* **2020**, *194*, 108847. [[CrossRef](#)]
137. Sun, S.H.; Hagihara, K.; Ishimoto, T.; Suganuma, R.; Xue, Y.F.; Nakano, T. Comparison of microstructure, crystallographic texture, and mechanical properties in Ti–15Mo–5Zr–3Al alloys fabricated via electron and laser beam powder bed fusion technologies. *Addit. Manuf.* **2021**, *47*, 102329. [[CrossRef](#)]
138. Chen, N.; Wan, Z.; Wang, H.P.; Li, J.; Yang, B.; Solomon, J.; Carlson, B. Effect of ambient pressure on laser welding of AlSi10Mg fabricated by selected laser melting. *Mater. Des.* **2022**, *215*, 110427. [[CrossRef](#)]

-
139. Wu, H.; Li, J.; Wei, Z.; Wei, P. Effect of processing parameters on forming defects during selective laser melting of AlSi10Mg powder. *Rapid Prototyp. J.* **2020**, *26*, 871–879. [[CrossRef](#)]
 140. Dharmadhikari, S.; Basak, A. Evaluation of Early Fatigue Damage Detection in Additively Manufactured AlSi10Mg. In Proceedings of the 2021 International Solid Freeform Fabrication Symposium, Virtual, 5–27 July 2021; University of Texas at Austin: Austin, TX, USA, 2021.